LONDON, METEOROLOGICAL OFFICE.

Met.O.15 Internal Report No.62.

A model of drizzle growth in warm, turbulent, stratiform clouds. By NICHOLLS,S.

London,Met.Off.,Met.O.15 Intern.Rep.No.62, 1985,30cm.Pp.47;20 pls.17 Refs.

METEOROLOGICAL OFFICE
London Road, Bracknell, Berks.

MET.O.15 INTERNAL REPORT

Number 62

A Model of Drizzle Growth in Warm, Turbulent, Stratiform Clouds

by S. Nicholls

November 1985

Cloud Physics Branch (Met.O.15)

1. INTRODUCTION

It has long been known that even shallow layers of warm (ie. whose temperature is everywhere >0°C), stratiform cloud are capable of producing drizzle which reaches the ground. Mason (1952) refers to observations where drizzle was observed to fall from a cloud only a few hundred metres deep. Nicholls (1984, referred to as N84) presented observations made with modern airborne particle-sizing instrumentation in which significant amounts of drizzle fell from cloud only 450m deep. In this and other studies (eg. Brost et al, 1982), the settling of drops under gravity has been found to make a significant contribution to the vertical transport of water through the cloud topped boundary layer. Drizzle should therefore be quantified and included in models attempting to predict the behaviour of sheets of stratiform cloud. However, as Mason (1952) pointed out, the production of precipitation sized particles by shallow layers of cloud is incompatible with the simplest models of drop growth since growth rates due to condensation and coalescence are so slow that a drop would fall out of the cloud long before attaining the size necessary to survive the fall to the ground. But, as he also recognised, theory could be reconciled with observation if turbulent diffusion could be shown to extend the residence time of some of the drops within the cloud. Using a crude representation of turbulent motion within the cloud together with the limited knowledge of cloud structure then available, Mason was able to estimate the probability of an individual drop remaining within the cloud for a given length of time. He concluded that including the effects of vertical turbulent motions could extend the lifetimes of sufficient numbers of drops for sufficiently long to explain the existence of precipitation from shallow cloud.

Today, the processes causing droplet growth are better understood (eg. the stochastic nature of drop coalescence) and have been more accurately quantified (eg. the probability that droplet pairs will coalesce). More recently this has been matched by a dramatic improvement in observing techniques. Measurements of turbulence and drop size spectra over a wide range of radii are now made on an almost routine basis (eg. N84; Nicholls and Leighton, 1985, referred to as NL). These measurements confirm that

turbulent diffusion is potentially an important factor in determining the vertical distribution of even quite large drops (r ~ 100 μm) since updraughts exceeding the terminal velocities of such drops (~ $1ms^{-1}$) are regularly observed penetrating deep within stratocumulus layers. However, despite these advances, little progress in modelling the growth of precipitation in such clouds has been reported since Mason's original paper.

This paper describes an attempt to construct a model of large drop growth within a fairly realistic representation of a turbulent cloud layer. The development of the drop size distributions (dsd's) is calculated explicitly as a function of height which therefore yields quantitative information which may be compared with observations.

The main aims of the study are twofold. Firstly, to construct a model to help determine whether the observed distributions of precipitation sized drops are consistent with the observed cloud structure and our current knowledge of droplet growth processes. Secondly, to use the model to investigate the sensitivity of precipitation growth to various parameters including cloud depth and turbulence intensity.

A central feature of the model is the method used to represent the effects of turbulence, which retains the stochastic nature of the actual vertical motion field in a much more realistic way than has hitherto been attempted in models containing explicit microphysical calculations. In most previous models the dynamics of the reference volume or parcel are grossly simplified. A common approach is to calculate spectral evolution within a single Lagrangian parcel whose vertical movement is either restricted to an arbitrarily defined trajectory or one which also includes a response to buoyancy accelerations. However, in a fully turbulent environment (which includes most clouds), such a description is only valid for a short period of time which is small compared to the local Lagrangian integral timescale, τ_L. Over longer times, the essential random nature of the turbulent velocity field means that the integrity of the original parcel is progressively lost i.e. the 'lifetime' of the parcel is related to the local turbulence characteristics. This connection is often

disregarded in Lagrangian parcel models where drop growth is calculated within a single parcel framework over considerable periods of time, which essentially assumes that τ_L is very large. In fact estimates of τ_L from measurements in stratocumulus (see section 6.1) are typically only a few minutes. Although some single parcel models admit the possibility of mixing between parcels with differing histories, the possibility of encountering parcels representing a complete spectrum of previous development and the probability of such events occurring are not considered within a consistent framework nor is any attempt made to render these consistent with the ensemble averaged statistics of the turbulent velocity field. The dynamical framework of such models therefore remains completely deterministic and although the effects of the stochastic nature of drop interactions on small scales may be included through the stochastic coalescence equation (SCE), the stochastic nature of turbulent diffusion (present in almost all clouds) is ignored. This general criticism may be levelled at almost all previous attempts at modelling the microphysical evolution of clouds and represents a fundamental deficiency. While use of the SCE allows certain 'lucky' drops to experience growth rates significantly greater than average because certain interactions have a small, but nevertheless finite, possibility of occurring, so turbulent diffusion also enables other 'lucky' drops to be carried upwards within the cloud, significantly extending their lifetimes within regions rich in smaller drops. Only a very small fraction need to be transported upwards a significant distance to have a marked effect since the efficiency of the coalescence process is strongly increased by the presence of a few, larger collector drops. Note that this process is entirely different from the enhanced growth mechanism envisaged by Tennekes and Woods (1973) where increased turbulence was expected to increase the chance of droplet pairs coalescing ie. to increase the effective collision cross-section.

The model described below includes representations of both stochastic coalescence and stochastic turbulent diffusion. Furthermore, the latter is achieved in a manner consistent with the observed characteristics of the turbulent cloud layer. Following a general overview of the structure of the model, the turbulent diffusion and drop growth schemes are described in detail. Comparisons with previous results are made whenever possible and

the assumptions and limitations of the model are assessed critically. A simulation of a real case is then described and compared with observations. The sensitivity of the results to the assumptions made, to the intensity of turbulence and to variations in cloud depth and water content are also examined.

2. A GENERAL DESCRIPTION OF THE MODEL

The basic structure of the model is depicted schematically in Fig 1. A steady, horizontally homogeneous turbulent layer lies between two impervious boundaries and is divided into a number of equally spaced levels of thickness δz. In the upper part of this turbulent region and adjacent to the upper boundary lies the cloud layer. Vertical diffusion within the turbulent region is represented by a model which decomposes the motion into an ensemble of constant velocity trajectories connecting any two levels in times which are multiples of the basic timestep, δt. The probability of each trajectory occurring, p, is related to the observed statistics of the turbulent layer. Three of the many possible trajectories which terminate at one particular level are illustrated in Fig 1. Clearly the sum of all the probabilities must be unity at each level ($\Sigma p = 1$). Some of the trajectories lie completely or partially within the cloud layer and along these it is possible to calculate the development of the drop size distributions which are stored at each level in a number of discrete radius classes. The spectral evolution along a trajectory includes a representation of condensational or evaporative effects, growth by stochastic coalescence and the effects of gravitational settling between neighbouring levels. The mean dsd is defined at each level by summing the contributions from all the trajectories terminating there, weighted by their probability of occurrence, p. The model therefore predicts the mean dsd's at each level within the cloud layer at each timestep. Solutions for the next timestep are developed in terms of the same ensemble of trajectories (the turbulence statistics do not vary with time) originating from solutions obtained at previous times. The model is run forward in time from prescribed initial conditions until a steady state is eventually reached where drop growth is exactly balanced by gravitational settling.

The component parts of the model are now described in detail.

3. THE TURBULENT DIFFUSION MODEL

3.1 Description of the basic method

The method used to simulate turbulent diffusion is based on the integral equation, or IE, method (Pasquill & Smith, 1983). This stochastic representation is related to the Markovian random walk technique (Thomson, 1984), but by introducing probability distribution functions and integrating over all possibilities rather than explicitly following several thousand individual trajectories, is computationally much faster. Coupled diffusion and stochastic coalescence calculations are therefore a feasible proposition. As with the random walk method, the IE technique places no restrictions on the velocity distributions which can be used (actual measurements can be used directly) and because the Lagrangian integral scale of the turbulence can be varied as a function of position, boundaries can be specified in a relatively natural way.

The description of turbulent diffusion in the IE method is analogous to that of Browman motion on a molecular scale. The velocity of a marked fluid element or parcel, which is determined by a random process, is assumed to remain unchanged for a time t, but is then altered in an event in which all Lagrangian memory (or history of previous motion) is lost. The parcel and its properties are then indistinguishable from the mean state. The probability of an event occurring is related to the local value of the Lagrangian integral scale, τ_L. The probability of an event occurring in a time interval t is t/τ_L. Note how this description is fundamentally different to that employed in a single parcel model.

To illustrate how the evolution of a vertical concentration profile may be determined, suppose there exists some initial concentration distribution, $C_o(z)$, of an inert tracer which follows the air motions. In a time δt which is small compared with τ_L at all levels, the fluid elements composing the turbulent layer can reasonably be considered to move with unchanged velocities and the new concentration profile will be given by

$$C_1(z) = \int_{\text{all } z'} C_o(z')\, Q_1(z,z')\, dz' \qquad (1)$$

or, when considering discrete vertical levels,

$$C_1(z) = \sum_{z'} [\, C_o(z')\, Q_1(z,z') \,] \qquad (2)$$

Here,

$$Q_1(z,z') = \int_{w_-}^{w_+} D(w,z')\, dw \qquad (3)$$

where D(w,z') is the probability density function of the vertical velocity, w, at height z' and

$$w_+ = (z - z' + \delta z/2) / \delta t \qquad (4)$$

$$w_- = (z - z' - \delta z/2) / \delta t \qquad (5)$$

To simplify the notation, an operation R(p) may be defined which yields the concentration profile which would result from an initial concentration $C_k(z)$ if the velocities were to remain unchanged for a time $p\delta t$. Then

$$R(p)\ C_k(z) \equiv \sum_{\text{all } z'} [\, C_k(z')\ Q_p(z,z')] \qquad (6)$$

where now $w_+ = (z - z' + \delta z/2)/p\delta t$ (7)

and $w_- = (z - z' - \delta z/2)/p\delta t$ (8)

Eqn (2) may therefore be written as

$$C_1(z) = R(1)\, C_o(z) \qquad (9)$$

After a time interval δt, the probability that an event has occurred is $\delta t/\tau_L$. If τ_L is constant in both space and time, as in steady, homogeneous turbulence, and if

$$1/L \equiv \delta t/\tau_L \qquad (10)$$

the concentration profile at time $2\delta t$ will be given by

$$C_2(z) = (1 - \tfrac{1}{L})\, R(2)\, C_o(z) + \tfrac{1}{L}\ R(1)\, C_1(z) \qquad (11)$$

The first term represents the contribution from all those parcels which have not yet experienced an event and continue to move with their original velocities. The second term includes the contributions from that fraction of parcels which did experience an event at $t = \delta t$ when the concentration profile was given by $C_1(z)$ and have subsequently moved with new velocities for a time δt. After n intervals, the concentration profile is given by

$$C_n(z) = (1 - \tfrac{1}{L})^{n-1}\ R(n)\, C_o(z) + \sum_{p=1}^{n-1} \left[\frac{1}{L}\ (1 - \frac{1}{L})^{p-1}\ R(p)\, C_{n-p}(z) \right] \qquad (12)$$

The first term still accounts for that diminishing proportion of parcels which have not yet undergone an event and are still moving with their original, unchanged velocities. The second term includes all possible combinations of parcels which have experienced one or more events in the interval $n\delta t$ expressed in terms of the concentration profiles at intermediate times $C_i(z)$, i=1 ... n-1.

If τ_L is now allowed to vary with position, $\delta t/\tau_L$ and hence L become functions of z. When a parcel moves from z' to z with an unchnged velocity in a time $n\delta t$, the chance of an event occurring becomes

$$\prod_{i=1}^{n} (1/L_i) \qquad (13)$$

where L_i is the local value of L at height $z-i(z-z')/n$. Note that δt must still remain less than τ_L at all locations for the motions to be properly resolved. Eqn (12) then becomes

$$C_n(z) = \sum_{\text{all } z'} \left[\prod_{i=1}^{n-1} (1-1/L_i)\ \ Q_n(z,z')\, C_o(z') \right] + \sum_{\text{all } z'} \left[\sum_{p=1}^{n-1} \left\{ \frac{1}{L_p} \prod_{i=1}^{p-1} (1-1/L_i)\, Q_p(z,z')\, C_{n-p}(z') \right\} \right] \qquad (14)$$

where the two terms are interpreted as before. The solution, $C_n(z)$, is therefore built up from a sum of weighted contributions from all possible Lagrangian trajectories. A certain proportion of the concentration existing at a particular level at time $(n-p)\delta t$, which is determined by the local velocity probability distribution, will set off at a constant velocity to arrive at another level at time $n\delta t$. Only a fraction of those initially setting off will actually complete this trajectory. This fraction depends on the values of the local Lagrangian timescale which are encountered along the trajectory. The others experience one or more events and 'forget' about the initial concentration distribution, $C_{n-p}(z)$. As time proceeds and n increases, the total contribution to $C_n(z)$ from $C_o(z)$ therefore decreases as

$$\prod_{i=1}^{n-1} (1-1/L_i) \to 0$$

This implies that the series expressed in eqn (14) may be truncated. Indeed this is necessary if eqn (14) is to be evaluated for large values of n since the number of terms in the second part of the equation increases approximately as n^2 and every previous solution $C_i(z)$, i=0 to n-1, must be retained. If only contributions from the preceding r timesteps are retained i.e. all explicit memory of concentration profiles prior to the time $(n-r)\delta t$ is lost, eqn (14) becomes

$$C_n(z) = \sum_{\text{all } z'} \left[\prod_{i=1}^{r-1} (1-1/L_i)\, Q_r(z,z')\, C_{n-r}(z') \right]$$

$$+ \sum_{\text{all } z'} \left[\sum_{p=1}^{r-1} \left\{ \frac{1}{L_p} \prod_{i=1}^{p-1} (1-\frac{1}{L_i}) \right\} Q_p(z,z')\, C_{n-p}(z') \right] \quad (15)$$

for all $n > r$. The coefficients Q and L are now independent of n and may be evaluated as functions of z and z' for each of preceding r timesteps. Eqn (15) is then

$$C_n(z) = \sum_{\text{all } z'} \sum_{p=1}^{r} P_p(z,z')\, C_{n-p}(z') \quad (16)$$

where $P_p(z,z')$ is a three dimensional matrix of fixed coefficients which express the probability of a parcel, originating from level z' at time $(n-p)\delta t$, moving with a constant velocity to level z at time $n\delta t$.

Starting from an initial concentration profile $C_o(z)$, the subsequent r solutions are determined using eqn (14) which involves recalculating the coefficients on each timestep. When n=r, the coefficients $P_p(z,z')$ are retained. For solutions when $n > r$, eqn (16) is used, the coefficients remain the same, and only the preceding r solutions need be saved.

3.2 The treatment of boundaries

A general feature of turbulent flows adjacent to a boundary, whether a solid wall or a density interface, is that the integral length and time scales of the flow decrease as the distance from the boundary decreases. Since the scheme described above allows τ_L to vary with height, the boundaries can be specified in a natural way. Eqn (15) shows that if L approaches the value 1 along any part of a trajectory, the probability of a parcel continuing on unaffected becomes very small as the coefficient $(1-1/L) \to o$, unless p=1. Thus, if a parcel trajectory encounters a region where L is small, the probability of an event occurring is so high that little memory of previous concentration history is retained. A region where $L \approx 1$ therefore provides an effective barrier to all those trajectories whose duration exceeds δt. The only contributions to $C_n(z)$ in this region arise from $C_{n-1}(z)$, indeed if L=1 everywhere, eqn (15) reduces to

$$C_n(z) = \sum_{\text{all } z'} Q_1(z,z')\, C_{n-1}(z') \quad (17)$$

and there are only contributions from the preceding timestep. An impervious boundary can therefore be specified by reducing the value of L to around one, coupled with some form of reflection applied to the contributions arising from diffusion from the preceding timestep.

Reflection of these trajectories which would otherwise cross the boundary is achieved by calculating the time (ie. the fractional timestep) taken to reach the boundary where an event is assumed to occur. For the remainder of the timestep, the parcel is assumed to move with a velocity given by the appropriate positive or negative half of the probability density function D(w,z).

The main drawback of specifying boundaries in this way is that where L $\approx$ 1, $\delta t \approx \tau_L$, which conflicts with the assumption that $\delta t \ll \tau_L$ everywhere. The motions in this region are therefore poorly resolved, a disadvantage of the IE method compared with random walk techniques where the timestep can be adjusted along an individual trajectory in response to the local value of τ_L. Other disadvantages associated with the specification of boundaries are discussed in section 3.4 below.

3.3 Choice of grid interval and timestep

The values of δz and δt should be chosen to be sufficiently small to resolve the motions as well as possible, yet sufficiently large to limit the number of computations to feasible proportions.

The largest fractional change in τ_L encountered during a single timestep is given by

$$\frac{\delta \tau_L}{\tau_L} = \frac{d\tau_L}{dz} \cdot \frac{w_m \delta t}{\tau_L} \qquad (18)$$

where w_m is the maximum vertical velocity (disregarding sign) and the motion will be well resolved if $^{\delta}\tau_L/\tau_L \ll 1$. Using eqn (10), this may be written

$$\frac{\delta \tau_L}{\tau_L} = \frac{\delta L}{L} = \frac{dL}{dz} \frac{w_m \delta t}{L} \ll 1$$

$$\text{or} \qquad \delta t \ll \left(\frac{dL}{dz}\right)^{-1} \frac{L}{w_m} \qquad (19)$$

Similarly, the fractional change encountered when moving between adjacent levels is

$$\frac{\delta \tau_L}{\tau_L} = \frac{1}{L} \frac{dL}{dz} \delta z$$

leading to the condition

$$\delta z \ll L \left(\frac{dL}{dz}\right)^{-1} \qquad (20)$$

for well resolved motion. Furthermore, if artifical numerical diffusion due to too large a grid spacing is to be avoided then

$$\delta z \ll w_m \delta t \qquad (21)$$

Eqns (19)-(21) may be combined to give

$$\delta z \ll w_m \delta t \ll L \left(\frac{dL}{dz}\right)^{-1} \qquad (22)$$

However the number of computations sets a lower bound on δz. The number of terms required to calculate the next concentration profile by eqn (16) is approximately

$$T = \left(\frac{Z}{\delta z}\right)^2 r \qquad (23)$$

where Z is the maximum height of the domain. Also, to ensure that eqn (16) is not truncated prematurely,

$$r \delta t > \tau_{Lm} \qquad (24)$$

where τ_{Lm} is the maximum value within the domain. Eqns (23) and (24) imply

$$\delta z > \left(\frac{\tau_{Lm}}{T \delta t}\right)^{1/2} Z \qquad (25)$$

and the maximum permissible value for T will determine the lower bound on δz.

The values of δt and δz chosen must satisfy both eqns (22) and (25). Some examples are considered below.

3.4 Examples of the Method in Use

a) Homogeneous, isotropic turbulence

In this special case, the velocity distribution and τ_L are the same everywhere. In this example, the velocity probability density function was specified as

$$D_1(w) = \frac{15}{16 w_m}\left(1 - \frac{w^2}{w_m^2}\right)^2 \quad \text{for } -w_m \leq w \leq w_m$$
$$= 0 \quad \text{for } |w| > w_m. \qquad (26)$$

The velocity distribution is symmetrical about a zero mean and has $\sigma_w = 0.378\ w_m$ (Pasquill and Smith, 1983). The other specified parameters are listed below:

$w_m = 1.0\ ms^{-1}$ $\qquad$ $\delta t = 1$ min

$\tau_L = 6$ min $\qquad$ $\delta z = 10$ m

$Z = 2$ km (200 levels)

The series in eqn (15) was truncated after 15 timesteps (r=15) so that explicit memory of the initial conditions is lost after a time $2.5\ \tau_L$. These values satisfy both eqns (22) and (25) if $T \approx 2.5\ 10^5$.

The evolution of the concentration profiles from an initial horizontal sheet $2\delta z$ thick is shown in Fig 2 together with the velocity distribution, $G_1(w)$. The profiles vary smoothly and the spreading of the concentration conforms closely to the results of Taylor's (1921) theory with an exponential Lagrangian correlogram:

$$\sigma_z/\sigma_w\tau_L = \{2\ (t/\tau_L + \exp[-t/\tau_L] - 1)\}^{1/2} \qquad (27)$$

The evolution of σ_z and values from eqn (27) are shown in Fig 3 together with the asymptotic limits from eqn (27) which are that $\sigma_z \propto t$ when $t \ll \tau_L$ and $\sigma_z \propto t^{1/2}$ when $t \gg \tau_L$. The model gives a good representation of diffusive spreading although truncating the series at r = 15 causes σ_z to be slightly underestimated for $t > 2.5\ \tau_L$. The model domain limits are reached at $t = 20\ \delta t$. In this example where L is constant with height, it

is straightforward to show that the total concentration is exactly conserved. This is confirmed by the numerical results within the limits set by rounding errors.

b) Inhomogeneous turbulence

In the following examples, boundaries are imposed by varying τ_L with height as suggested in section 3.2. The chosen vertical variation of L ($= \delta t/\tau_L$) is shown in Fig 4. The distribution is symmetrical about the midpoint and is used in all the examples presented below. Some observational evidence supporting such a distribution is given in section 6.1.

Two vertical velocity distributions are used in the examples: the symmetrical distribution from eqn (26) shown in Fig 2 with $w_m = 1.0\ ms^{-1}$, denoted $G_1(w)$, and an arbitrarily defined distribution, $G_2(w)$, shown in Fig 5. Both distributions have a zero mean and similar width ($\sigma_{w1} = 0.38\ ms^{-1}$, $\sigma_{w2} = 0.36\ ms^{-1}$) but $G_2(w)$ is negatively skewed (skewness = -0.68).

G(w) is not allowed to vary with height because of the additional complications this would incur, requiring at least the introduction of 'bias' or small non-zero mean vertical velocities. This is a general problem for stochastic diffusion models which admit varying velocity distributions and is necessary to avoid unrealistic concentration gradients building up. The compensating velocities required may be related to the vertical gradients of moments of G(w) (for further discussion see e.g. Legg & Raupach, 1982; Thomson, 1984). In any case, variations in G(w) with height are not thought to be of central importance to the growth of precipitation sized drops, especially since observations show that large variations in σ_w are not commonly found within stratiform cloud layers except very close to cloud top (eg NL). However, the absence of any reduction of σ_w close to the boundaries in the model does lead to some unrealistic concentration increase there for reasons discussed below.

Fig 5 shows the evolution of the concentration profile from an identical initial state to that shown in Fig 2. All the other parameters remain as in that example except that L(z) is as shown in Fig 4 giving 72 levels and the velocity distribution $G_2(w)$ is used. The concentrations are scaled by C_* which would be the value obtained if the initial total concentration was distributed uniformly amongst all levels. As time proceeds, the concentration profile develops smoothly, the asymmetry resulting from the form of $G_2(w)$. When $t \geq 10\ \tau_{Lm}$, the profile tends towards a stedy, well-mixed shape (which is independent of the initial concentration distribution) where the concentration is distributed approximately evenly throughout the domain. However, close to the boundaries the profiles display unrealistic maxima due to the poor resolution of trajectories within this region. Eqn (22) is only satisfied when

$$L \gg \frac{dL}{dz} \quad w_m \quad \delta t \qquad (28)$$

and in this example $(dL/dz)\ w_m\ \delta t \approx 2.5$ within a distance of ~10 δz from the boundary. Fig 4 shows that L is less than this value within a distance of ~ 5 δz of the boundary which closely matches the region where the concentration increase is observed. The problem is most acute immediately adjacent to the boundary where L is smallest, $\delta t = \tau_L$, and the motion is clearly not properly resolved. Even so, only the two levels closest to the boundaries are strongly affected, concentrations throughout the rest of the domain are constant to within 10% and in the central region (> 10 δz from boundaries) to within 1%. As suggested by eqn (28), the size of these concentration maxima (for a given specification of L(z)) are reduced if w_m or δt are decreased, provided eqn (21) remains satisfied. This suggests that allowing σ_w to decrease near the boundaries, in line with observations, could reduce these unrealistic maxima considerably. An associated limitation is also that total concentration is no longer conserved, varying typically by a few per cent per hour of modelled time. However, these drawbacks should be kept in perspective and $C \rightarrow C_*$ over the great majority of the domain. The method described above clearly offers a more powerful and realistic description of turbulent diffusion capable of being coupled to microphysical calculations than has been tried before. As a final illustration that the model is capable of reproducing known

characteristics, Fig 6 compares the concentration profiles at $t = 20\ \delta t$ from the example (shown in Fig 5) which uses $G_2(w)$ and an identical run with velocity statistics specified by $G_1(w)$. The upward displacement of the concentration maximum in conditions where G(w) is negatively skewed is clearly apparent.

4. CLOUD MICROPHYSICS

Along any one of the ensemble of trajectories defined by the turbulent diffusion model, an initial distribution of drops within a parcel will be modified by condensation and evaporation, coalescence and the vertical transport of drops by gravitational settling between adjacent layers.

The dsd's are defined in terms of concentrations in 49 classes on a logarithmically increasing scale. A drop in the ith class has a mass given by

$$m_i = m_o\ 2^{(i-1)/2} \qquad (29)$$

so that successive classes contain drops whose radii charge by a factor $2^{1/6}$. A value of m_o was chosen so that the smallest class corresponds to r = 1.6 μm and the largest to r = 400 μm. As discussed by Jonas and Mason (1974), this representation enables a whole range of drop sizes to be covered with a reasonable number of classes and also enables the SCE to be solved in a reasonably rapid, accurate and economical way.

4.1 Condensation and evaporation in cloud

A rigorous treatment of condensational effects requires the calculation of the parcel saturation as a function of time together with detailed knowledge of the cloud condensation nucleus activity spectrum. Furthermore, the computation of saturation implies a complete specification of the thermodynamic state of the parcel as a function of time which, in a fully turbulent flow, is inextricably linked with the pressure and velocity fields. This alone would require a considerably more complex representation of turbulence than is considered here and the addition of

explicit microphysical calculations would render the problem computationally intractable. However, the main interest of this study is the growth of precipitation sized drops which permits considerable simplification.

It is well known that the relative importance of condensation and evaporation as mechanisms for drop growth in clouds declines rapidly for drops with $r \geq 25$ μm, so the growth of larger drops due to coalescence is largely independent of the local saturation (provided it is maintained close to unity). The growth rates of these larger drops are not sensitive to the manner in which the small ($r < 25$ μm) drops are formed, just to the resultant size distribution. The importance of condensation and evaporation lies not in influencing the growth rates of large drops directly, but in controlling the numbers and sizes of the smaller drops. Therefore, if the distribution of the numbers of these small drops can be externally specified in some way, the need for explicit calculations involving the parcel saturation may be avoided.

Observational studies of the microphysical structure of stratiform clouds often show a well-defined unimodal small drop spectrum which varies in a fairly straightforward and repeatable manner throughout the depth of the cloud except when in close proximity to the boundaries (eg Slingo et al, 1982; N84; NL). Furthermore, variations about the mean at a given level in horizontally uniform conditions are quite limited eg. differences in spectra between updraughts and downdraughts are small (again, if measurements close to cloud top or cloud base are avoided). Because of these features, it is possible to approximate the small drop distributions measured on particular occasions fairly realistically by a single empirical function which varies with height above cloud base (an example is given in section 6.1 below).

In the model, the concentrations within the first i_* classes are therefore set to the appropriate prespecified values which depend upon the current height of the trajectory (i_* also varies with height). This procedure largely determines the liquid water content of the parcel which is contained mostly in the smaller drops ($i \leq i_*$) and which is little

affected by the addition of larger drops. Thus on a rising (descending) trajectory, the parcel liquid water content increases (decreases) according to the specified rate and the effects of droplet growth (loss) due to condensation (evaporation) are represented in a realistic way, through changes in the small drop spectrum.

While this representation is admittedly crude, it has the advantage of extreme simplicity and because it is based on observations, always ensures that realistic distributions of smalldrops are used in the coalescence calculations. The main disadvantages are that this empirical description requires detailed observational input which is valid only for that set of conditions prevailing when the measurements were made, and that no account is taken of the possible effects of fluctuations in liquid water content along a trajectory since this is constrained to be close to the specified value. No explicit account of effects due to the entrainment of inversion air at cloudtop or possible enhancement of drop growth due to radiative cooling (Roach, 1976) are considered except insofar as these processes influence the mean (observed) small drop distributions.

4.2 Coalescence

Disregarding for the moment drops which fall from greater heights, drops appear in radius classes $i > i_*$ due solely to coalescence. The development of the drop size distribution within an air parcel along a trajectory is calculated by solving the SCE. According to Jonas and Mason (1974), the concentration of drops in class i, denoted g(i), changes with time according to

$$\frac{\partial}{\partial t} g(i) = \int_1^{i-2} c\, g(i_c)\, g(i')K(i_c,i')\, di' - \int_1^{\infty} g(i')g(i)K(i,i')\, di' \qquad (30)$$

where $c = (1 - 2^{(i'-i)/2})^{-1}$ and $i_c = i - 2 \ln c/\ln 2$. The first term of eqn (30) expresses the increase in g(i) due to the coalescence of two smaller drops while the second term represents the reduction in g(i) through coalescence with other drops. The values of the collection kernels, K, are the same as those used by Jonas and Mason (1974). Values of $g(i_c)$ are obtained by third order interpolation of ln(g) using the values of i nearest to i_c. Concentrations less than 10^{-31} m^{-3} are assumed to be zero.

The timestep which may be used to integrate eqn (30) is governed by the behaviour of the large radius tail of the size distribution: too large a value results in unacceptably large oscillations in the numbers of the largest drops, too small a value increases the number of computations. A method involving two timesteps was finally adopted as offering the best compromise between accuracy and speed. A basic timestep of δt_c = 20s was selected for all but the four classes containing the largest drops where a timestep of $\delta t_c/3$ was used. In tests, this gave results which were very similar to those obtained using a single 5s timestep but was considerably faster computationally. Tests on a closed parcel showed that total liquid water was conserved within 4% over a period of an hour during which time drops of radius ~300μm appeared and the total concentration was reduced by 30%. The length of the timestep δt_c was also chosen to be a submultiple of the diffusion timestep δt.

4.3 Gravitational settling:

Drops are assumed to fall with terminal velocities, w_T, given by Beard (1976) at a temperature of 5°C and a pressure of 900 mb. If a trajectory starts at a time $(n-p)\delta t$ and terminates at time $n\delta t$, the concentration of drops in each size class, g, is adjusted to account for gravitational settling occurring during the preceding timestep at the intermediate times $(n-j)\delta t$ where j=1 to p-1. This change in drop concentration is given by

$$\delta g = w_T \frac{\partial g}{\delta z} \delta t \qquad (31)$$

The vertical derivative is evaluated at the level reached halfway through the timestep and uses the appropriate mean values of g at the timesteps (n-j-1) and (n-j) which have already been determined. However, the mean concentration profiles at time δt are not yet known, so for the final timestep at the end of the trajectory, the distance fallen by the drops is calculated explicitly and the concentration in each class distributed amongst the appropriate levels as follows. If the parcel contains g_- drops in class i at time (n-1) δt and g_+ at time $n\delta t$, the number of drops falling from the parcel during the timestep is approximately

$$\delta g = \frac{1}{2} (g_- + g_+) w_T \delta t/\delta z$$

or

$$\delta g = (g_- + \alpha \frac{\delta t}{2}) w_T \frac{\delta t}{\delta z} \qquad (32)$$

where $\alpha \equiv (g_+ - g_-)/\delta t$ is the mean rate of increase in drop concentration during the timestep. If eqn (32) predicts $\delta g > g_+$, then δg is set equal to g_+ ie. all the drops have fallen out. In order to redistribute the drops falling out of the parcel amongst lower levels, the following assumptions are made. If $\alpha > 0$, drops represented by the first term of eqn (32) are assumed to have existed throughout the timestep and would therefore have fallen a distance $w_T\delta t$. Drops represented by the second term are assumed to have been formed at a constant rate during the timestep and are distributed between the final level of the trajectory and a distance $w_T\delta t$ beneath. If $\alpha < 0$, all the remaining drops are assumed to have been present throughout the timestep. By redistributing the drops in this way at each level, the concentration profile at time $n\delta t$ can be determined for each size class. Although this procedure incurs some artificial numerical spreading of the concentration, especially when $w_T \delta t/\delta z \ll 1$, this is always much smaller than the diffusive effects of the modelled turbulent velocity field in all realistic cases. No transport between adjacent levels of drops in classes $i \leq i_*$ is allowed. This is consistent with the assumption that this region of the dsd is controlled by condensation and evaporation associated with vertical motion and is already specified as described in section 4.1.

4.4 Drop size distributions beneath cloudbase

In principle, the dsd's could be calculated at all levels below cloudbase in exactly the same way as described above for the in-cloud levels, except that because the parcels would be strongly subsaturated on at least part of their trajectories, evaporation would potentially be the most important process affecting the dsd at all radii and would need explicit consideration. This could be implemented since the parcel relative humidity could be obtained by requiring suitable thermodynamic quantities to be conserved along subcloud trajectories. Unfortunately, extending the calculations to the complete ensemble of trajectories in both the cloud and subcloud layers is prohibited by the number of calculations

this would require (see section 5). A simpler approach was therefore taken, designed mainly to provide a reasonable initial dsd to those trajectories commencing below cloudbase but terminating within the cloud layer.

Drops are assumed to fall from cloudbase with a velocity w_T through a static, dry adiabatic subcloud layer of constant specific humidity chosen to give saturation at cloudbase. The drops are assumed to be non-interacting ie. coalescence is ignored in comparison to evaporative effects. This is reasonable since the evaporative decay rates are quite large even for the largest drops and because the total number density is very rapidly reduced as the smaller drops are evaporated completely within a few metres of cloudbase. The changing radius of a drop initially located at cloudbase is calculated as a function of time by solving an approximate form of the growth equation (eg. Rogers, 1979).

$$r \frac{dr}{dt} = (s-1)f_v/(F_K + F_D) \qquad (33)$$

where s is the ambient saturation ratio, f_v the ventilation coefficient (Pruppacher and Klett, 1978) and F_K, F_D are slowly varying functions of temperature and pressure. Also,

$$\frac{dz}{dt} = - w_T(r) \qquad (34)$$

and since both s(z) and $w_T(r)$ are known, eqns (33) and (34) can be solved to give r(z). By repeating this calculation for initial radii on the size class boundaries, drops contained in each class at cloudbase can be redistributed into the appropriate (smaller) classes at a lower level. By summing the contributions from each of the classes, the size spectrum resulting from a steady state dsd at cloudbase may be found at any subcloud level.

All parcels rising into the cloud layer are initialized with a dsd calculated by this method at a distance z_v below cloudbase. The choice of z_v is not critical (the sensitivity of the cloud layer results to this choice is discussed in section 6.2) provided it is greater than a few metres, which ensures most drops with r < ~10μm are totally evaporated, and less than ~ 100m where significant modification at all radii means the

spectra no longer representative of conditions just beneath cloudbase. A value of z_v = 15m gives acceptable results and is used in most of the examples discussed below.

5. THE COMPLETE MODEL

The turbulent motion field is decomposed into an ensemble of trajectories as described in section 3 and the evolution of the dsd's along them is calculated as described in section 4. The mean dsd's for the next timestep are obtained, as a function of height, by solving an equation similar to eqn (16) except that the scalar concentration C(z) is replaced by the drop size spectrum S(i,z):

$$S_n(i,z) = \sum_{\text{all } z'} \sum_{p=1}^{r} P_p(z,z') S'_{n-p}(i,z') \qquad (35)$$

Here $S'_{n-p}(i,z')$ represents the drop size distribution which has evolved from an initial value $S_{n-p}(i,z')$ along the trajectory between levels z' and z and between times (n-p) δt and nδt. However, as discussed in section 3, the turbulent diffusion scheme tends to produce unrealistic concentration maxima close to the boundaries of the domain ie. at cloudtop. To avoid this causing a corresponding build up of liquid water, which could significantly affect the microphysical interactions, mass conservation is enforced at each model level. This is achieved by concurrently computing the vertical distribution of a scalar quantity which is initially constant at all levels. From this a correction factor $\beta_n(z)$ can be derived which ensures the recovery of this initial profile at all subsequent times. If $C_o(z) = 1$ everywhere initially, then

$$\beta_n(z) = \frac{C_{n-1}(z)}{C_n(z)} \qquad (36)$$

With this correction, eqn (35) becomes

$$S_n(i,z) = \beta_n(z) \sum_{\text{all } z'} \sum_{p=1}^{r} P_p(z,z') S'_{n-p}(i,z') \qquad (37)$$

which provides the basis for all the solutions discussed below.

However, with realistic conditions the number of trajectories implied by eqn (37) is still too great to permit explicit microphysical calculations along each one. Even with the simplifications discussed in section 4, solving the SCE (eqn 30) involves calculating about i_m^2 separate terms every timestep δt_c where i_m is the largest size class containing drops (typically ~40). In the example discussed in section 3.4b, the total number of possible trajectories contributing to the solution at the next timestep is $T \approx 6\ 10^4$. If the cloud layer is allowed to occupy the top 30 levels and the dsd's are only calculated within this region (necessitating the simplified treatment of subcloud layer dsd's discussed in section 4.4), T is reduced by a factor of ~3. Since the averae duration of a trajectory is ~ 7 δt (r = 15 in this example), the total length of all the trajectories, 7 Tδt ~ 100 days if δt = 1 min. Thus each timestep would require eqn (30) to be solved for a total time of ~ 100 days involving ~ 4.10^5 steps (if δt_c = 20s) each consisting of ~ 1600 terms. This amount of computation is currently not feasible, so further simplifications had to be sought.

A reduction by a factor of about two is achieved by reducing r from 15 to 10 since both the numbers and average duration of the trajectories are reduced. However, a much greater reduction was achieved by calculating dsd evolution along only selected trajectories and interpolating the remainder. In most examples discussed below, values at the two levels adjacent to the boundaries and every subsequent third level were computed using contributions from the immediately preceding and every subsequent third solution, as illustrated in Fig 7. Concentration was assumed to vary linearly between selected vertical levels (z') and also at the same level between selected times (p'). Since P is defined for all values of z' and p' (for each z), the $P_p(z,z')$ at each of the selected points (crosses in Fig 7) are amended to include weighted contributions from neighbouring points. Thus in the example shown in Fig 7

$$P_p'(z,z') = \sum_{i=-2}^{2} \sum_{j=-2}^{2} a_{ij}\, P_{p'+j}(z,z' + i\delta z) \quad (38)$$

where $a_{ij} = (1-|i|/3)(1-|j|/3)$. The summations in eqn (37) now run over this restricted set of points, which in this case reduces T by a further factor of ~15. A comparison of steady state concentration profiles calculated using these simplifications with those obtained using the complete description (Fig 8) shows that the solutions are not significantly degraded.

In the example under discussion, T is reduced by these additional simplifications to manageable proportions (~ 800) and the total length of all the trajectories is ~60 h per timestep (1 min).

6. RESULTS

6.1 Description of the case to be modelled

The case chosen to test the model is based on an observational study of extensive, horizontally uniform stratocumulus cloud over the North Sea on 22 July 1982. Details of the aircraft data obtained on this occasion have already been published in N84 and NL. The comprehensive nature of this set of data which includes measurements of turbulence structure as well as cloud droplet distributions in the range $2 < r < 400$ μm (using ASSP and 2D-Cloud probes) and liquid water content (Johnson-Williams) make this a good choice for testing the model.

The mean depth of the cloud was determined to be 450 m, the maximum horizontally averaged liquid water content was about 0.6 gm^{-2} and drizzle was observed below cloud down to the lowest flight level (90m asl). Further details are listed in Table 1 and in the papers referenced above.

a) Specification of turbulence structure:

The modelled turbulent motion is specified by the vertical velocity distribution function, G(w), which is assumed to remain constant with height, and the vertical variation of L(z), which is related to that of τ_L (eqn 10). Since Lagrangian measurements are notoriously difficult to make,

and in any case could not be attempted during the experiment in question, the usual practice of making assumptions to relate them to Eulerian quantities is followed here.

If an aircraft flies through the turbulent, cloudy layer at a speed V, the integral time scale measured in a reference frame moving with the aircraft, τ_A, will be given by ℓ/V where ℓ is the integral length scale. At the same time, the Lagrangian integral timescale, τ_L, will be approximately ℓ/σ_w where σ_w is a characteristic turbulence velocity scale. The ratio of these two timescales, τ_L/τ_A is therefore of order V/σ_w. The timescale τ_A may be estimated directly from the aircraft vertical velocity measurements since

$$\tau_A \approx \frac{1}{2\pi} \cdot \frac{1}{f_A} \qquad (39)$$

where f_A is the frequency at which the peak of the vertical velocity spectrum, $f\,S_w(f)$ occurs. An expression for τ_L is therefore given by

$$\tau_L \approx \frac{V}{2\pi\,\sigma_w\,f_A} \qquad (40)$$

A survey of the theoretical and the very limited observational estimates of the ratio $\tau_L\sigma_w/V\tau_A$ in a variety of flows by Pasquill and Smith (1983) implies a 'best' value somewhat less than one (~ 0.7), although the uncertainties are considerable. Thus eqn (40) might overestimate τ_L although it will be shown that the final results are not particularly sensitive to changes of this magnitude.

With a timestep of 1 min dictated by the constraints discussed in section 3.3, the values of L resulting from the measurements of f_A and eqn (40) are shown in Fig 9. These are found to increase downwards beneath cloud top in a similar manner to that implied by the measurements of f_A by Caughey et al (1982) in similar, radiatively driven stratocumulus. It is also encouraging that the derived values of τ_L ~ 6 min in the lower parts of the cloud layer imply that vertically moving elements will maintain their identity throughout a considerable fraction of the depth of the cloud ($\tau_L\,\sigma_w$ ~ 130 m with $\sigma_w = 0.36$ ms^{-1}) which is consistent with the observation of 'adiabatic' regions (ie. measurements consistent with unmixed ascent from cloudbase) deep within the cloud layer.

The variation of L within the model domain was chosen to match the observations within the cloud and to provide suitable boundaries. Two representations used are also shown in Fig 9.

A domain consisting of 74 levels with a 15m spacing was selected for most runs with the cloud layer occupying the uppermost 29 and L(z) specified by the solid curve in Fig 9. L(z) is reflected in the lower half of the domain to provide a reasonable lower boundary. The vertical velocity distribution function, G(w), was determined directly from measurements made at a height of 730m and is similar to the $G_1(w)$ distribution shown in Fig 2 although it is slightly negatively skewed (skewness ≈ -0.1) and $\sigma_w = 0.36$ ms^{-1}. Other measurements confirm these values are characteristic of this cloud layer (N84). The series in eqn (37) was truncated at r = 10 (ie. after approximately 1.5 τ_{Lm}) for most runs. The sensitivity of the solutions to this choice is discussed in section 6.2.

b) Specification of the small drop distributions:

It was found that a single empirically fitted curve gave a reasonably good approximation to the shape of the horizontally averaged spectra measured with the ASSP ($2 < r < 24$ μm) at each of the levels where horizontal runs were made (730m, 610m, 475m). Shifting this curve towards larger radii with increasing height above cloudbase was found to approximate the observed mean spectra quite well at all measurement levels. As discussed in section 4.1, these spectra are defined only for drops in classes $i \leq i_*$ and i_* is here defined as

$$i_* = i_{peak} + 5 \qquad (41)$$

where i_{peak} is the class containing the peak of the dsd. The numbers of drops in each class are reduced by a constant fraction (up to 10%) in the top 30m of the cloud to match the observations reported by NL. This is believed to reflect the effects of dry air entrainment on the mean dsd's at these levels.

Comparisons between this specification and observations (from the analysis presented in NL) are shown in Fig 10. Both the mean dsd's at 730 m and 475 m are well reproduced as is the variation of the total concentration (N), the mean volume radius (r_v) and the liquid water content (ρ_ℓ) with height. The figure also shows the values of these parameters once larger drops have been formed and a steady state has been reached. In comparing these quantities, it should be noted that the observations include only drops for which $r \leq 24$ μm in calculating N and r_v while the Johnson-Williams probe probably underestimates the liquid water content of drops with $r > 30$ μm.

6.2 Results and sensitivity tests

The model was run forward in time from the initial conditions described above. At first there are no drops larger than those in class i_* at any level, but drops subsequently grow by coalescence, are transported vertically by turbulent diffusion and eventually fall out of the cloud. Eventually, after 1-2 hours of simulated time, equilibrium is attained at all levels and the mean dsd's reach steady values. The initial and equilibrium dsd's at four selected levels within the cloud layer are shown in Fig 11. The vertical variation of the total concentration, mean volume radius and liquid water content at equilibrium were shown in Fig 10.

The dsd's shown in Fig 11 are typical of those produced by the model. In this example, the largest drops formed are about 250 μm in radius and drops in radius classes up to 100 μm are found in concentrations of at least 1 m^{-3} throughout the cloud layer. Furthermore, the concentrations of drops larger than a certain size ($r \approx 30$ μm in this example) increase downwards from cloud top towards cloudbase where they are a maximum. These features are compared with observations in section 6.3 below.

A number of sensitivity tests were carried out using the current example to assess the possible effects on the results of the various assumptions and simplifications discussed in earlier sections. These included:

i) Computing spectral evolution along every trajectory, not just those selected by the reduced method described in section 5 (ie. i=j=o in eqn 38).

ii) Truncating the series in eqn (37) after 13 preceding solutions rather than 10 (ie. r = 13).

iii) Defining the small drop distributions over a slightly reduced size range ($i_* = i_{peak} + 4$, cf. eqn 41).

iv) Changing the vertical grid interval from 15m to 22.5m.

v) Changing the specification of L to that shown by the dashed curve in Fig 9.

vi) Changing the depth of the subcloud layer by specifying the lower boundary to be just (60m) beneath cloudbase.

vii) Initialising trajectories commencing below cloudbase with a dsd calculated using z_v = 30m rather than 15 m (see section 4.4).

None of these changes was found to produce significant changes in the calculated mean, equilibrium dsd's. At cloudbase, the concentration of drops in a fairly large radius class (r = 141 μm) were found to vary by no more than ±20% from that obtained in the reference run shown in Fig 11. The size of these changes can be judged by the fact that the difference between the concentrations at this radius at the two lowest levels shown in Fig 11 (ie. 0m and 120m) is almost exactly 20%.

In contrast, altering the vertical velocity distribution, G(w), can produce relatively large changes in the equilibrium dsd's. Further runs were made with the turbulent vertical velocities multiplied by a series of constant factors to give σ_w = 0.25, 0.5 and 2.0 times the reference value

σ_{wref} (= 0.36 ms^{-1}) and also with no vertical diffusion (σ_w = 0). Other parameters were kept the same as in the reference example. The resulting equilibrium dsd's at cloud top and cloudbase are shown in Fig 12.

The most obvious result is that increasing σ_w leads to a greatly increased concentration of larger drops at all levels in the cloud. For example including turbulence with $\sigma_w = \sigma_{wref}$ increases the radius of the largest drops found at cloudtop from 71 μm (no turbulence) to 224 μm and from 141 μm to 252 μm at cloudbase (see Table 2). Furthermore, the concentration of drops at 126 μm radius at cloudbase is increased by a factor of 4.10^7. These effects increase progressively as the turbulence intensity is increased and are very much larger than the 20% changes observed during the sensitivity tests discussed earlier.

The distributions of smallest drops also respond to these changes in σ_w, especially lower down in the cloud layer (as seen at cloudbase in Fig 12), although these changes are not as marked as those at larger radii. In classes $i > i_*$ (~ 5 μm at cloudbase in this example) and for which $r < 20$ μm, the concentrations decrease slowly with increasing radius and are found to be relatively insensitive to changes in σ_w provided $\sigma_w > 0$. At slightly larger radii, $r > 20$ μm, the concentrations decrease more quickly, this rate of decrease being proportional to σ_w. These changes are caused by a combination of factors.

i) As σ_w is increased, a larger fraction of the trajectories terminating at each level originate below cloudbase where the drop concentrations, especially in the smaller radius classes, are strongly reduced by evaporation. The small drop concentrations in the examples with $\sigma_w > 0$ are therefore all smaller than the corresponding values when $\sigma_w = 0$.

ii) The greatly increased concentration of larger drops at higher σ_w leads to a greater depletion of smaller drops by coalescence.

iii) The relatively crude representation of condensation and evaporation effects along trajectories tends to cause a discontinuity in the dsd's at class $i = i_{*max}$ where i_{*max} is the largest value of i_* at any level within

the cloud. This arises because at some level the numbers of drops in classes $i \leq i_{*max}$ are fixed. These values are subsequently transmitted throughout the rest of the cloud layer by diffusion, so the numbers of drops in classes $i_* < i \leq i_{*max}$ at other levels are influenced to some extent by the concentrations imposed at the level where $i_* = i_{*max}$. Thus although the effects of phase change are explicitly taken into account at any level by specifying concentrations in classes $i \leq i_*$, they also have an indirect influence on the concentrations in all classes up to and including i_{*max}. However, drops in the next largest class can only be formed by coalescence and this rigid division can give rise to a rather abrupt change.

Returning to Fig 12, concentrations in the range 5μm < r < 20 μm at cloudbase are relatively insensitive to σ_w variations because the losses incurred through processes i) and ii) are compensated by the diffusive flux (iii). However, in the range 20 μm < r < ~ 50 μm, process iii) is no longer operative (i_{*max} occurs at r = 20 μm in this example), increasing σ_w increases the losses due to i) and ii), so the numbers of drops are depleted. This leads to the discontinuous feature at r = 20 μm. Although this feature is an artifact of the model formulation, sensitivity tests have showed that the large drop concentrations (r > ~ 50 μm) are quite insensitive to its presence. It should also be recalled that because the small drop spectra ($i \leq i_*$) are defined empirically by reference to observations in conditions whose $\sigma_w \approx \sigma_{wref}$, tests at other values of σ_w cannot reflect any modification to this part of the spectrum which might result.

As the number and size of the larger drops increases, so too does their influence on the vertical flux of liquid water due to gravitational settling or rainfall rate given (eg. N84) by

$$R(z) = \int_i \left(\frac{4}{3}\pi\rho_w g(i,z)\, r(i)^3\, w_T(i) \right) \equiv \int_i Y(i,z) \qquad (42)$$

Both g(i,z) and Y(i,z) are plotted in Fig 13 for runs in which $\sigma_w = 0$ and $\sigma_w = \sigma_{wref}$. In the case with $\sigma_w = 0$, the maximum value of Y occurs at the same radius (~ 20 μm) at all levels in the cloud. When $\sigma_w = \sigma_{wref}$, the increased numbers of larger drops make a significant contribution which

increases in importance downwards from cloudtop until at cloudbase, this contribution is dominant. This is consistent with the observational results discussed in N84. Only when significant levels of turbulence are included does this bimodality appear. As σ_w is increased the size of the peak at large radii increases relative to that at smaller radii and also occurs at progressively larger radii. Table 2 shows that the peak value of Y at cloudbase moves from r = 20 μm when σ_w = 0 to r = 79 μm when σ_w = 2 σ_{wref}. However, this table also shows that the concentration depletion in the range 20 μm < r < 50 μm, discussed above, largely offsets this increased contribution to the total rainfall rate at cloudbase and actually causes the total to decrease at the higher σ_w values.

Beneath cloudbase, the dsd's are calculated by the method described in section 4.4. Fig 14 shows the results obtained at four subcloud levels from the reference example discussed above. As anticipated, the concentrations of small drops are strongly reduced within a short distance of cloudbase while the larger drops are progressively less affected at a given level because of their larger volume/surface ratios and their greater fallspeeds. In this case, where cloudbase is at a height of 380m (Table 1), only drops which were initially larger than 140μm radius survive the fall to the surface.

6.3 Comparisons with observations

Observations of the dsd's were made at a number of levels both in and below cloud during a three hour period around noon, as described in N84. The horizontally averaged dsd's measured at flight levels approximately 100 m below cloud top (730 m) and 100m above cloud base (475m) are shown in Fig 15. The observed concentrations have been redistributed into the model size classes by assuming that the log (concentration μm^{-1}) varies linearly between adjacent measured size bins. Small drop concentrations (r < 25 μm) are derived from ASSP data, the larger particles from the 2D-cloud probe. The absence of an overlap between these two parts of each spectrum at r ≈ 25 μm is believed to be caused by the 2D-probe undercounting smaller particles. This is a known deficiency related to the limited resolution imposed by the size of the photodetectors, but is believed to become

relatively insignificant for drops with r > ~ 50 μm (Ouldridge, 1982). The observations are terminated once the concentration falls below a minimum level of detectability (set at 1 count per size bin per 5 min flying time) which corresponds to ~ 1 m^{-3} per model class for drops in the range 60 μm < r < 200 μm.

The curves in Fig 15 show the corresponding modelled dsd's for these two levels from both the reference example and the case with σ_w = 0. The results from the model which includes turbulent diffusion agree reasonably well with the observed concentrations of larger drops (given that the measured concentrations are probably underestimated in the range 25 μm < r < 50 μm) especially when compared with the results when σ_w = 0 which grossly underestimate the concentrations of the larger drops at all levels. However, the reference model still produces fewer large drops than were observed, especially in the lower levels of the cloud. Some specific comparisons (listed in Table 3) show that in the class at r = 126 μm (arrowed in Fig 15), drops were observed in concentrations of 150 m^{-3} at 475 m while the reference model yields only 3.5 m^{-3}. Nevertheless, this figure is an increase of a factor of 10^8 over the case where σ_w = 0. Similarly, the largest drops appearing in measurable quantities (> 1 m^{-3} $class^{-1}$) at the two levels are both smaller than observed when $\sigma_w = \sigma_{wref}$, but are seriously underestimated when σ_w = 0.

The sensitivity tests discussed earlier showed that changing those parameters by amounts consistent with observational uncertainty would be insufficient to produce significantly better agreement with the observed large drop concentrations. However, two possibilities remain.

First, the conditions used in the reference example actually underestimate both the measured mean volume radius and the liquid water content at almost all levels (see Fig 10), as confirmed by the integrated liquid water path,

$$£ = \int_{\text{cloudbase}}^{\text{cloudtop}} \rho_\ell(z)\, dz \qquad (43)$$

listed in Table 3. Furthermore, the observed values are possibly slightly underestimated since the Johnson¬Williams probe is believed to underestimate the contributions from larger drops (see section 6.1) which become increasingly important near cloudbase. The model derived quantities include all drop sizes.

Second, cloud thickness was found to vary with a standard deviation of ± 65 m about the mean value of 450 m. Two further runs were therefore carried out to test whether increasing r_v and the liquid water content closer to the observed levels could result in the formation of significantly greater concentrations of large drops and to assess the sensitivity of the results to changes in cloud depth.

In run A, the same small drop spectral shape defined previously was shifted to slightly larger radii to give better agreement with the observed values of r_v and ρ_ℓ (see Fig 16 and c.f. Fig 10). This was also used in run B, where in addition, the values were extrapolated upwards to increase the cloud depth by 90m. This results in a maximum liquid water content of 0.8 gm^{-3} (Fig 16) which corresponds closely to the highest observed value. In both cases, the specification of the other parameters was unchanged from the reference run discussed previously. These two runs therefore correspond to the maximum likely liquid water content for a cloud of the same depth (450m) as the average observed value (run A) and for a cloud with the maximum observed depth (540m, run B). Run A provides a closer approximation to the observed mean state than the reference run, while run B represents the thickest cloud consistent with the observations, as reflected in the values of £ listed in Table 3.

Results from the two runs are shown in Fig 17. Both runs have significantly higher numbers of larger drops than the reference run (cf Fig 15) which are in better agreement with the observed concentrations, although the gap between the measured and predicted values at moderate radii (r ~ 50 μm) widens somewhat. Overall, run A predicts the

concentrations of the larger drops quite successfully at both levels while run B predicts numbers higher than the observed mean levels. However, run B does successfully predict the maximum sized drops, as listed in Table 3.

If, as seems likely, the conditions in which the observations were made varied between those specified during the reference run and those of run B with an average close to run A, the sensitivity of the model to changes in cloud depth and liquid water content is sufficient to explain the main features of the observed dsd's within the cloud.

As £ is increased, the liquid water flux due to gravitational settling (or the rainfall rate, R(z)) is predominantly carried by the larger drops whose concentrations increase most rapidly, as seen in Fig 18 (cf Fig 13). Because of this, R(z) is quite sensitive to £ as shown in Fig 19. As £ changes by a factor of 2 between the reference run and run B (see Table 3), the rainfall rate at cloudbase changes by a factor of 10. The results from the reference run and run A show reasonable agreement with the observed values in cloud (taken from N84), especially as R is approximately a fifth order moment of the size distribution. However, beneath cloudbase the vertical gradient of R(z) is much larger than the observed value, implying that the simple treatment of section 4.4 results in too rapid evaporation. The effects are seen more clearly in Fig 20 which compares modelled dsd's from run A at 300m and 90m with their observed counterparts. Although there are some similar features, for example at each level the concentrations at larger radii are progressively less reduced, the reduction in numbers at any given radius is much greater in the model than is observed. This is believed to be caused by ignoring the effects of turbulent diffusion in the subcloud layer. The evaporation of drops falling under gravity through an adiabatic layer is highly non-linear: in the examples above, all drops with r < ~ 140 μm at cloudbase are completely evaporated before falling the 380m to the surface while all the larger drops survive. If the stochastic effects of turbulent diffusion were included, then some drops would be transported downwards with velocities significantly greater than their terminal fallspeed. Reducing the time exposed to the ambient subsaturation in this way would mean that many drops which would otherwise have evaporated completely, will now reach the

surface. The inclusion of this process would be expected to lead to increased numbers of drops beneath cloudbase, reduced vertical concentration gradients and better agreement with observations. It is essentially the reverse of the process modelled in the cloud layer where diffusive effects lead to enhanced drop growth by prolonging the lifetimes of certain drops within the cloud.

7. DISCUSSION

The strong sensitivity of the rainfall rate to £ implied by the model suggests that this process could be the most important factor limiting the water content of thick cloud layers. The results for run B (see Fig 19) show that the effect of rainfall growth is to deplete the liquid water quite strongly within the cloud layer, at a rate given by

$$\frac{\partial R}{\partial z}(z) \approx -0.23 \text{ g m}^{-3} \text{ hr}^{-1}, \qquad (44)$$

with a corresponding moistening of the subcloud layer. However, the current model does not permit consequential changes to the total water budgets of either layer. Cloud liquid water is simply maintained by continually replenishing the numbers of small drops to prespecified levels. Therefore it is implicitly assumed in the model that the resupply of liquid water by vertical turbulent transport and continued condensation is always just sufficient to maintain the steady, specified levels of liquid water in the cloud. In reality, however, the upward turbulent water flux into the cloud layer is constrained by other considerations eg. the size of the surface water vapour flux, and it may not be possible to maintain the cloud liquid water against the losses due to coalesence and subsequent gravitational settling. In the case described in N84, both the rainfall rate and the upward water vapour fluxes through the subcloud layer were ~ 10^{-5} ms^{-1}, suggesting that steady values could have been maintained, but had the cloud thickened sufficiently (to give an average value of £ similar to that used in run B) it is unlikely that such a balance would have been possible. Then £ would have decreased with time, accompanied by changes in the small drop size distributions, leading to a reduction in the rainfall rate. The model is not capable of responding in such a manner, but nevertheless these results do suggest that to maintain a moderately thick

(> 500m) layer of cloud requires either large fluxes of water vapour into the cloud to balance the significant losses by rainfall or a significantly different microphysical structure to that employed in these examples to reduce the growth of precipitation sized drops. The latter category could include liquid water contents reduced further from the adiabatic values, narrower small drop spectra or colloidally more stable dsd's (higher concentrations of smaller drops in preference to fewer larger ones). In this regard, it is intended to model other cases with some of these different characteristics in future to assess whether the model is capable of reproducing the correct sensitivity.

Improvements to the model formulation could also be tried, in two areas in particular. Firstly, the trajectory calculations could be extended into the subcloud layer. The associated probabilities are already defined in the current version and only the response of the dsd's to ambient subsaturation would need to be included. This would be expected to lead to a more realistic representation of the dsd's below cloudbase, but the increased number of trajectories would incur a serious computational penalty. Secondly, the current extremely simple method of representing condensation/evaporation effects in cloud could be improved by differentiating between up- and downdraughts. ALthough this would allow the liquid water content to be correlated with vertical velocity as is observed (eg NL), it is expected that a greater benefit would be an improved representation of evaporation in downdraughts. As discussed in section 6.2 earlier, the current all-or-nothing approach in which drops in classes $\leq i_*$ respond to evaporative effects while those in classes $> i_*$ do not, results in rather discontinuous distributions especially around i_{*max}. A more realistic, gradual response in classes around i_* could alleviate this difficulty.

8. CONCLUSIONS

This paper describes how a stochastic model of turbulent diffusion can be combined with explicit calculations of drop growth due to stochastic coalesence to produce a model which is applicable to the study of precipitation growth in warm, layer clouds. With the small drop

distributions derived from observations, a steady state distribution of large drops is eventually achieved which represents a balance between growth by coalesence, transport by turbulent diffusion and loss by gravitational settling. The formulation enables the stochastic nature of the turbulent motion to be expressed in a much more realistic way than has hitherto been included in conjunction with explicit microphysical calculations of this type. Previously this important aspect of turbulent flows has often been entirely disregarded or treated in a statistically incomplete manner. The description employed here is consistent with measured turbulence statistics, reproduces known results reasonably closely and can be used to provide a framework for microphysical calculations.

The steady state concentrations of precipitation sized drops are found to be increased by some orders of magnitude when realistic levels of turbulence are included compared with an identical situation where $\sigma_w = 0$. This arises because a few particles have a relatively unlikely (but finite) chance of encountering a significantly higher than average proportion of updraughts. This leads to enhanced growth rates by extending their lifetimes within cloud and in some cases by recycling drops upwards through regions of higher liquid water content. This explains why even shallow layers of warm cloud can produce significant amounts of drizzle. Comparisons with observations show that the predicted concentrations and sizes of large drops are in good quantitative agreement with measurements without the need for adopting significantly different coalesence efficiencies from generally acecpted values or for considering alternative mechanisms for enhancing drop growth.

Tests using the model show that increasing the turbulence intensity results in increased concentrations of larger drops, but a much greater sensitivity is found to changes in cloud depth and liquid water content (as measured by the integrated water path, £). In particular, the rainfall rate increases strongly with £ suggesting that this process may be an important constraint on the liquid water content of thick cloud layers.

Further work is planned to investigate the response of these processes to changes in the small drop distributions and to compare results with other case studies to find out whether the model is capable of displaying the correct sensitivity.

Nicholls, S. 1984 N84 The dynamics of stratocumulus: aircraft observations and comparisons with a mixed layer model. Quart. J.Roy. Met. Soc., 110, 783-820.

Nicholls, S. & Leighton, J.R. 1985 NL An observational study of the structure of stratiform cloud sheets. Part I. Submitted to Quart. J.Roy. Met. Soc.

Ouldridge, M. 1982 The PMS 2-D array spectrometer system. M.O. 15 Internal Note No. 35. (Copy available in Met. Office Library).

Pasquill, F. & Smith, F.B. 1983 Atmospheric diffusion (3rd Edn). Ellis Horwood Ltd, Chichester, England.

Pruppacher, H.R. and Klett, J.D. 1978 Microphysics of clouds and precipitation. D. Reidel, Dordrecht, Holland.

Roach, W.T. 1976 On the effect of radiative exchange on the growth by condensation of a cloud or fog droplet. Quart. J.Roy. Met. Soc., 102, 361-372.

Rogers, R.R. 1979 A short course in cloud physics (2nd Edn). Pergamon Press. Oxford, England.

REFERENCES

Beard, K.V. 1976 Terminal velocity and shape of cloud and precipitation drops aloft. J. Atmos. Sci., 33, 851-864.

Brost, R.A., Wyngaard, J.C., and Lenschow, D.H. 1982 Marine stratocumulus layers. Part II: Turbulence budgets. J. Atmos. Sci., 39, 818-836.

Caughey, S.J., Crease, B.A., and Roach, W.T. 1982 A field study of nocturnal stratocumulus: II. Turbulence structure and entrainment. Quart. J.R. Met. Soc., 108, 125-144.

Jonas, P. and Mason, B.J. 1974 The evolution of droplet spectra by condensation and coalescence in cumulus clouds. Quart. J. Roy. Met. Soc., 100, 286-295.

Legg, B.J. & Raupach, M.R. 1982 Markov-chain simulation of particle dispersion in inhomogeneous flows: The mean drift velocity induced by a gradient in Eulerian velocity variance. Boundary Layer Meteorol. 24, 3-13.

Mason, B.J. 1952 Production of rain and drizzle by coalescence in stratiform clouds. Quart. J.Roy. Met. Soc., 78, 377-386.

Slingo, A., Nicholls, S., and Schmetz, J. 1982 Aircraft observations of marine stratocumulus during JASIN. Quart. J.Roy. Met. Soc., 108, 833-856.

Taylor, G.I. 1921 Diffusion by continuous movements. Proc. Lond. Math. Soc, Set 2, 20, 196-212.

Tennekes, H., & Woods, J.D. 1973 Coalescence in a weakly turbulent cloud. Quart. J.Roy. Met. Soc., 99, 758-763.

Thomson, D. 1984 Random walk modelling of diffusion in inhomogeneous turbulence. Quart. J.Roy. Met. Soc., 110, 1107-1120.

Average cloud top height	830 m
Average cloud base height	380 m
Cloud base temperature	10.8 C
Cloud top temperature	8.5 C
Cloud base pressure	980 mb

Table 1 Details of the case studied

	σ_w/σ_{wref}				
	0	0.25	0.5	1.0	2.0
Largest drop at cloudtop (radius, μm)	71	141	200	224	252
Largest drop at cloudbase (radius, μm)	141	200	224	252	252
Concn, in class at r=126μm at cloud top (m^{-3})	$1.8.10^{-16}$	$6.5.10^{-8}$	$1.4.10^{-4}$	$4.1.10^{-2}$	0.9
Concn. in class at r=126μm at cloudbase (m^{-3})	$1.0.10^{-7}$	$9.9.10^{-3}$	0.39	4.1	9.7
Radius of class containing peak rainfall rate at cloudbase (μm)	19.8	44.5	50	63	79
Rainfall rate at cloudbase (ms^{-1}) x 10^5	0.63	0.55	0.62	0.61	0.37

Table 2 Effects of changing σ_w on model results.

	Level (m)	'Reference' run $\sigma_w=0$	'Reference' run $\sigma_w=\sigma_{wref}$	Run A	Run B	Observations
Largest observable drop (radius, μm)	730	50	112	158	178	178
	475	71	141	178	224	224
Concn. in class at r=126 μm (m^{-3})	730	$1.9.10^{-11}$	0.45	13	86	7
	475	$3.5.10^{-8}$	3.5	132	575	150
£ (gm^{-2})	-	143	136	198	271	171

Table 3 Comparisons between model results and observations

List of Figures

Fig 10. Upper panels. Vertical variation of droplet concentration, N, mean volume radius, r_v, and liquid water content, ρ_ℓ, defined in the reference run at t=0 (——) and at steady state (...) compared with observations (●).
Lower panels. Comparisons of prescribed average small drop spectra (——) and observations (-·-·) at two levels in cloud (statistics from the measured spectra are indicated by ✖ in the upper panels). The relevant values of i_* are also indicated.

Fig 11. Equilibrium drop size distributions at four levels in the cloud layer. The initial distributions at the same four levels are shown displaced downwards twenty units for clarity.

Fig 12. Equilibrium drop size distributions at cloud top and cloud base with different values of turbulence intensity, σ_w.

Fig 13. Plots of drop concentration (left) and contribution to rainfall rate (right) as functions of size and height for two values of turbulence intensity, $\sigma_w = 0$ (upper figs) and $\sigma_w = \sigma_{wref}$ (lower figs).

Fig 14. Equilibrium drop size distributions at four subcloud layer levels from the reference run. The distribution at cloudbase is shown by the dashed curve.

Fig 15. Observed and modelled drop size distributions at z = 475 m and 730 m. Model results are shown with $\sigma_w = 0$ and $\sigma_w = \sigma_{wref}$.

Fig 16. Steady-state vertical variation of droplet concentration, N, mean volume radius, r_v, and liquid water content, ρ_ℓ, for runs A (——) and B (- - -) compared with observations (●).

Fig 17. Observed and modelled drop size distributions at z = 475m and 730m. Model results are shown from run A and run B ($\sigma_w = \sigma_{wref}$ in both).

Fig 18. Contribution to rainfall rate as a function of drop size and height for run B.

Fig 19. Rainfall rate as a function of height for the reference run, run A and run B compared with observations (- - ✖ - -). The position of cloudbase is indicated by a horizontal line on each curve.

Fig 20. Equilibrium drop size distributions at two levels below cloudbase (z = 300m and 90m) from run A compared with observations made at the same heights.

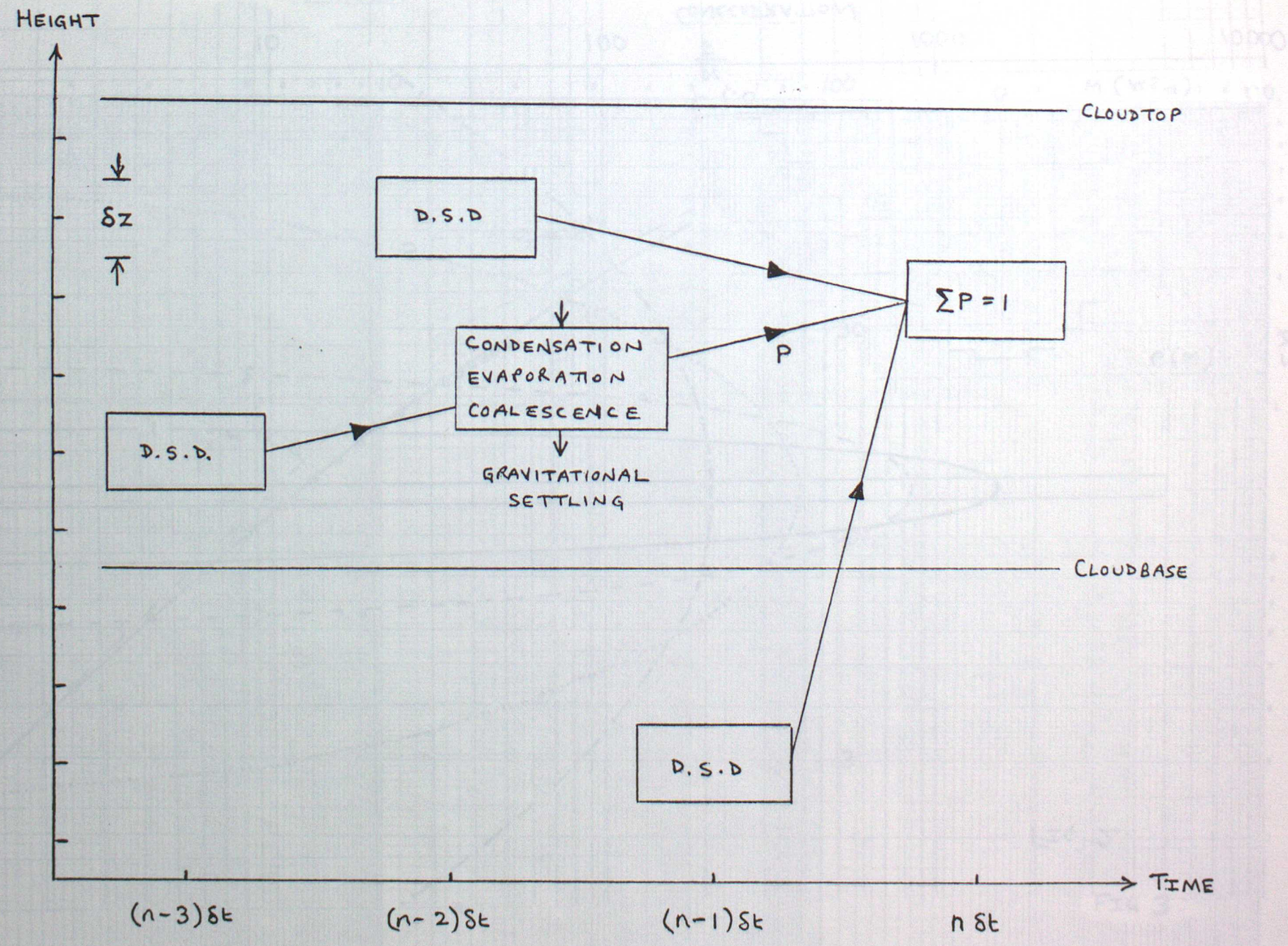
HEIGHT
CLOUDTOP
δz
D.S.D
ΣP = 1
CONDENSATION
EVAPORATION
COALESCENCE
P
D.S.D.
GRAVITATIONAL
SETTLING
CLOUDBASE
D.S.D
TIME
(n-3)δt
(n-2)δt
(n-1)δt
n δt

FIG 1

FIG 2

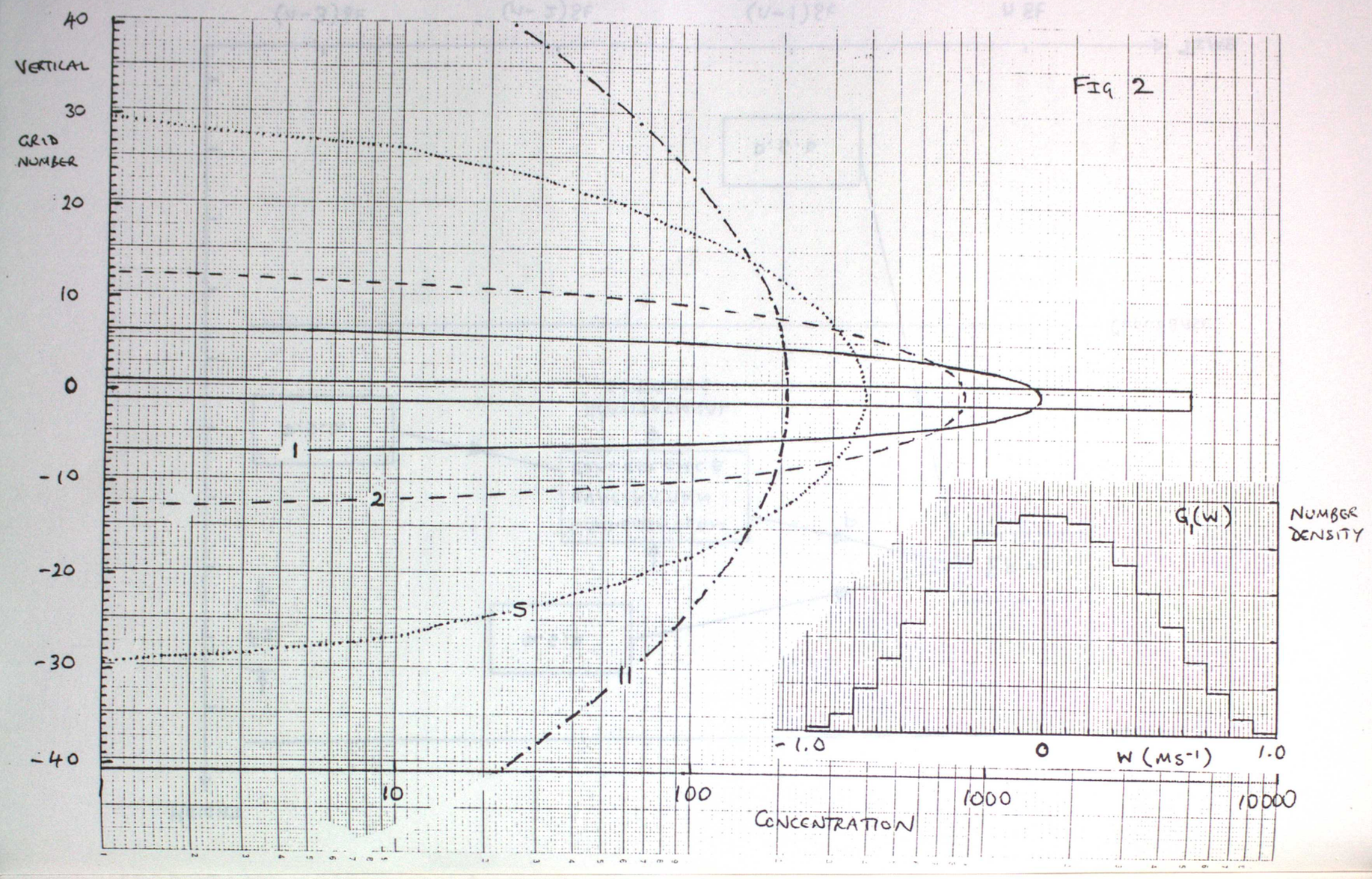
40
VERTICAL
30
GRID
NUMBER
20
10
0
-10
-20
-30
-40
1
2
5
11
10
100
1000
10000
CONCENTRATION
$G_1(W)$
NUMBER
DENSITY
-1.0
0
W (MS⁻¹)
1.0

FIG 3

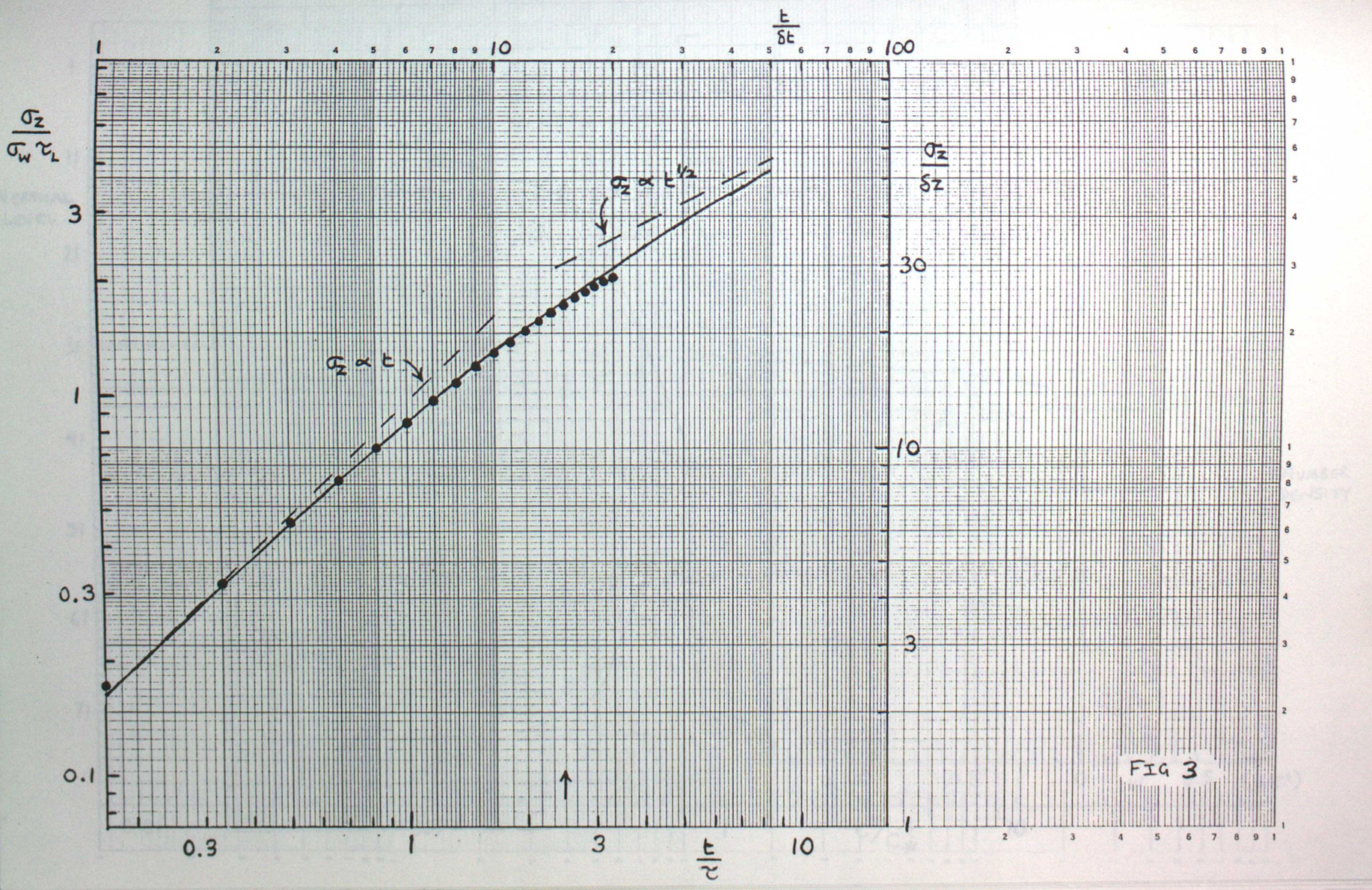
$\frac{t}{\delta t}$
$\frac{\sigma_z}{\sigma_w \tau_L}$
$\frac{\sigma_z}{\delta z}$
$\sigma_z \propto t^{1/2}$
$\sigma_z \propto t$
3
1
0.3
0.1
30
10
3
1
0.3
1
3
10
$\frac{t}{\tau}$

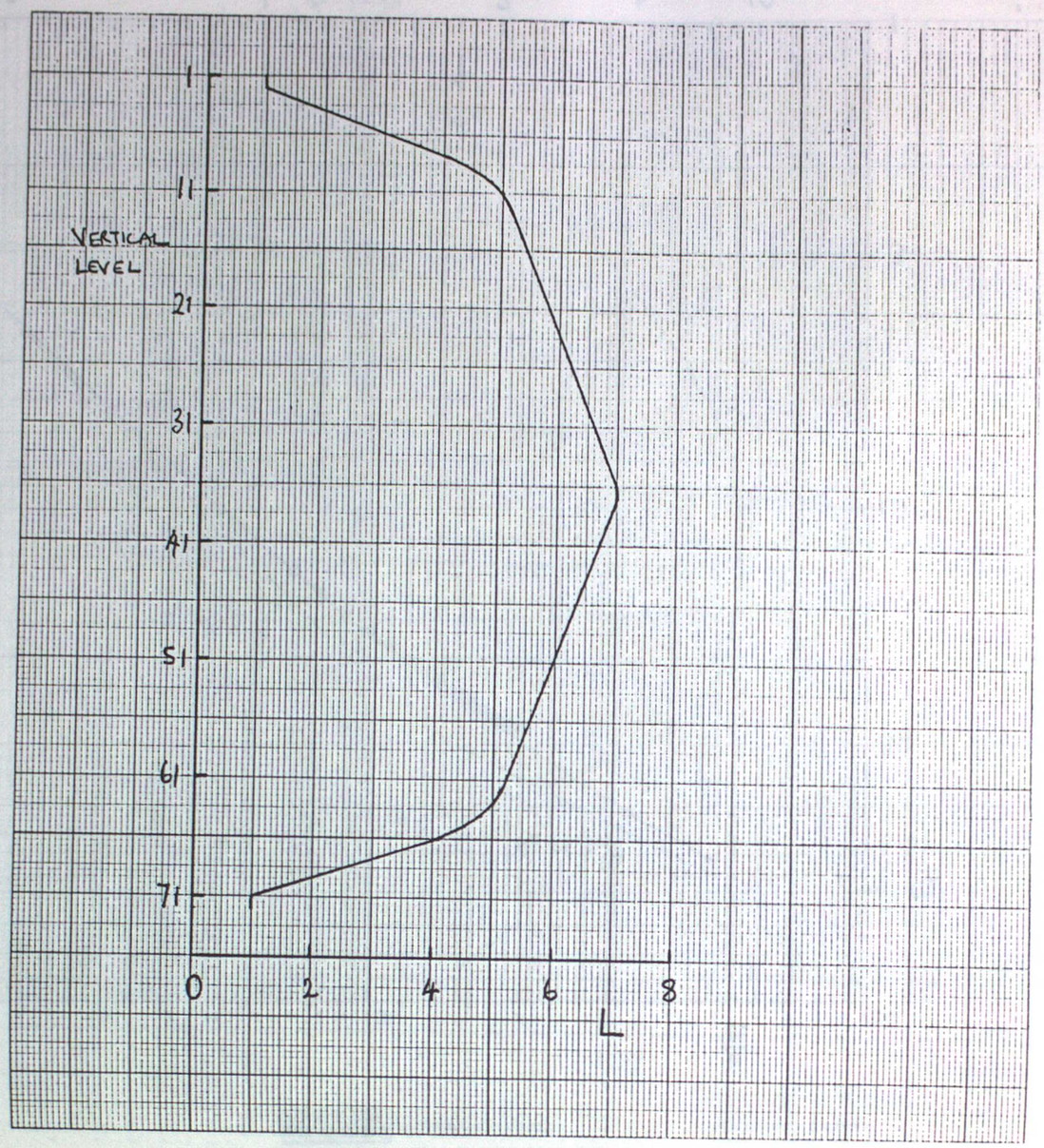

FIG 4

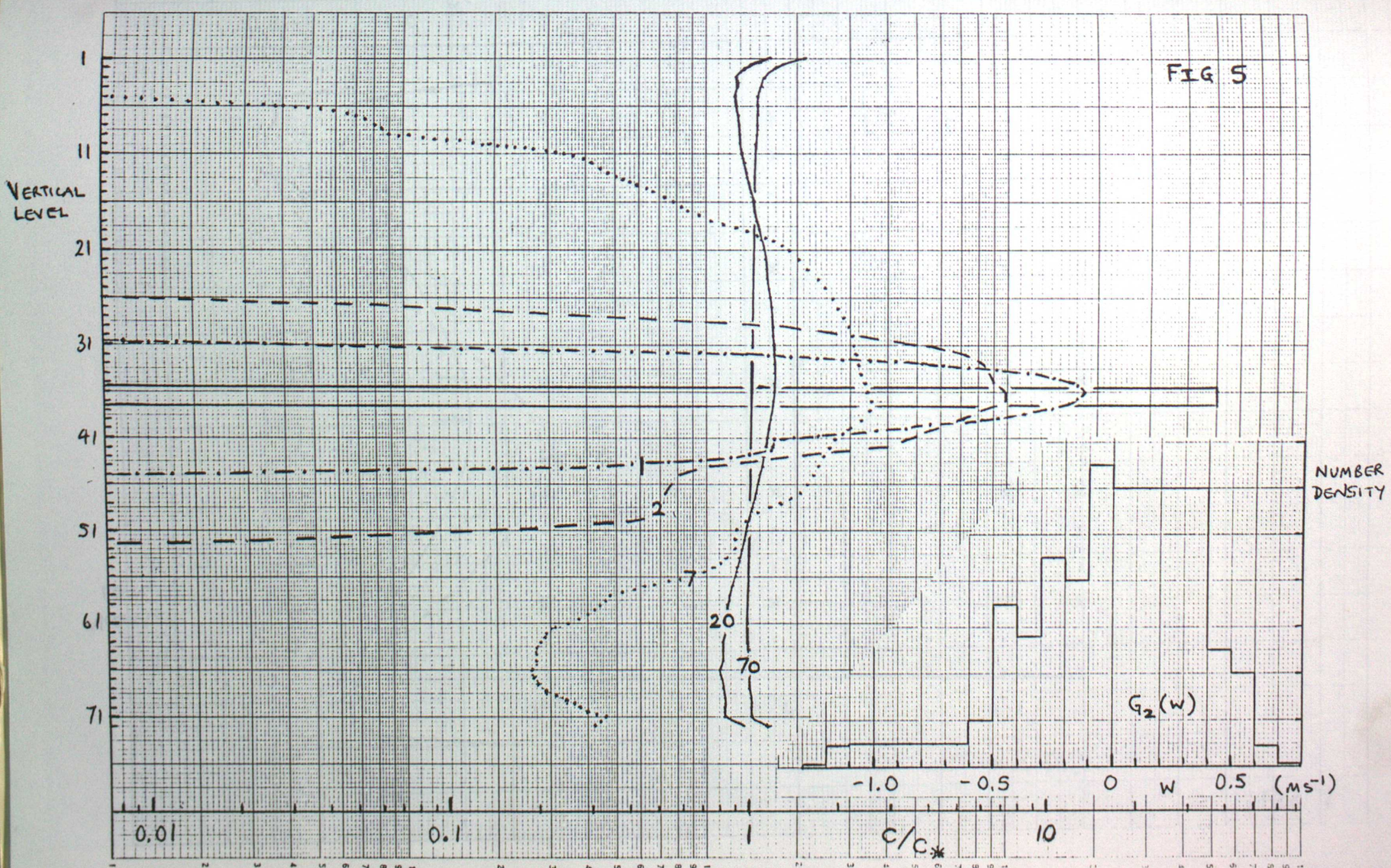

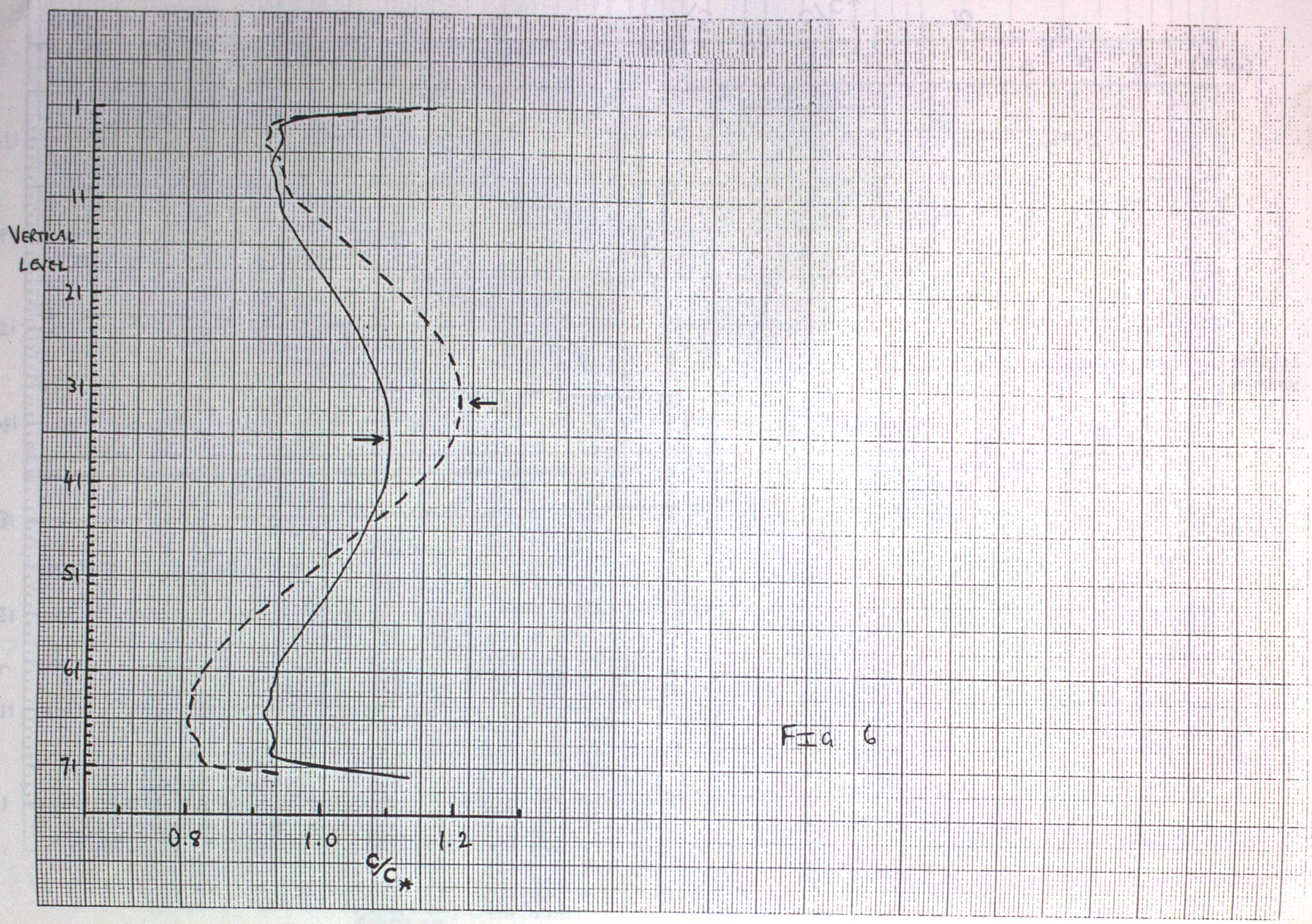
1
11
21
31
41
51
61
71
VERTICAL LEVEL
0.8
1.0
1.2
C/C*

FIG 6

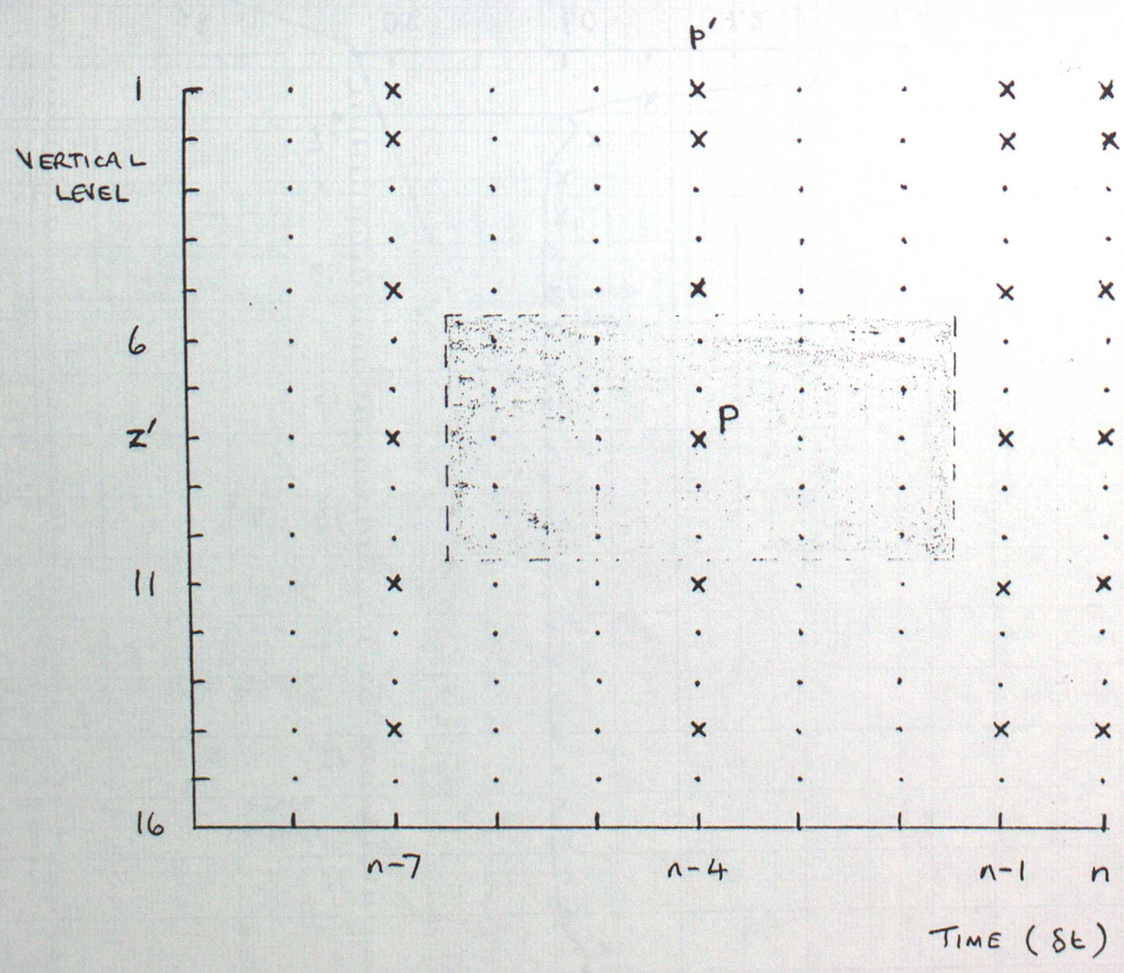
P'
1
6
11
16
VERTICAL LEVEL
z'
P
n-7
n-4
n-1
n
TIME (δt)

FIG 7

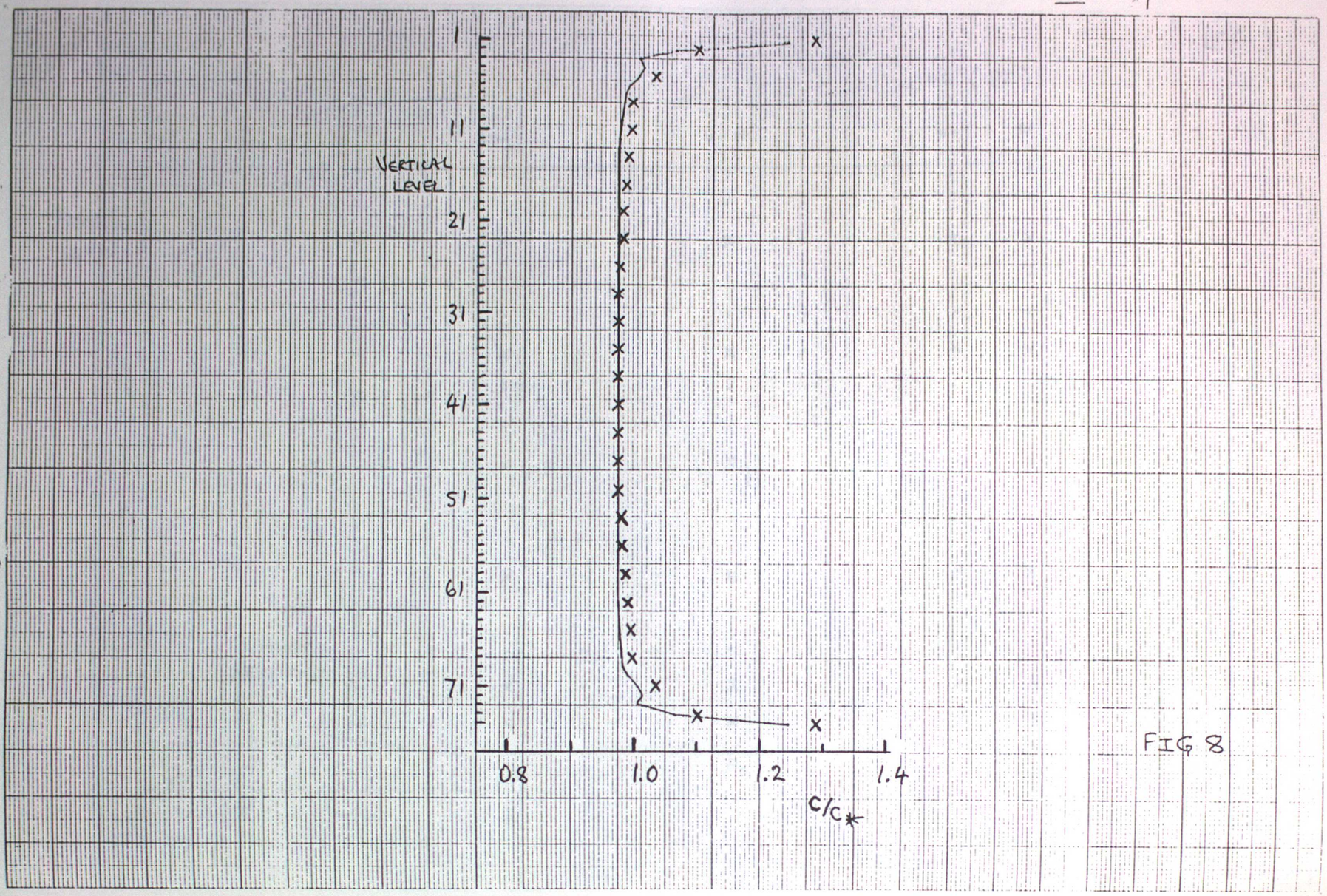
VERTICAL LEVEL
1
11
21
31
41
51
61
71
0.8
1.0
1.2
1.4
C/C*

FIG 8

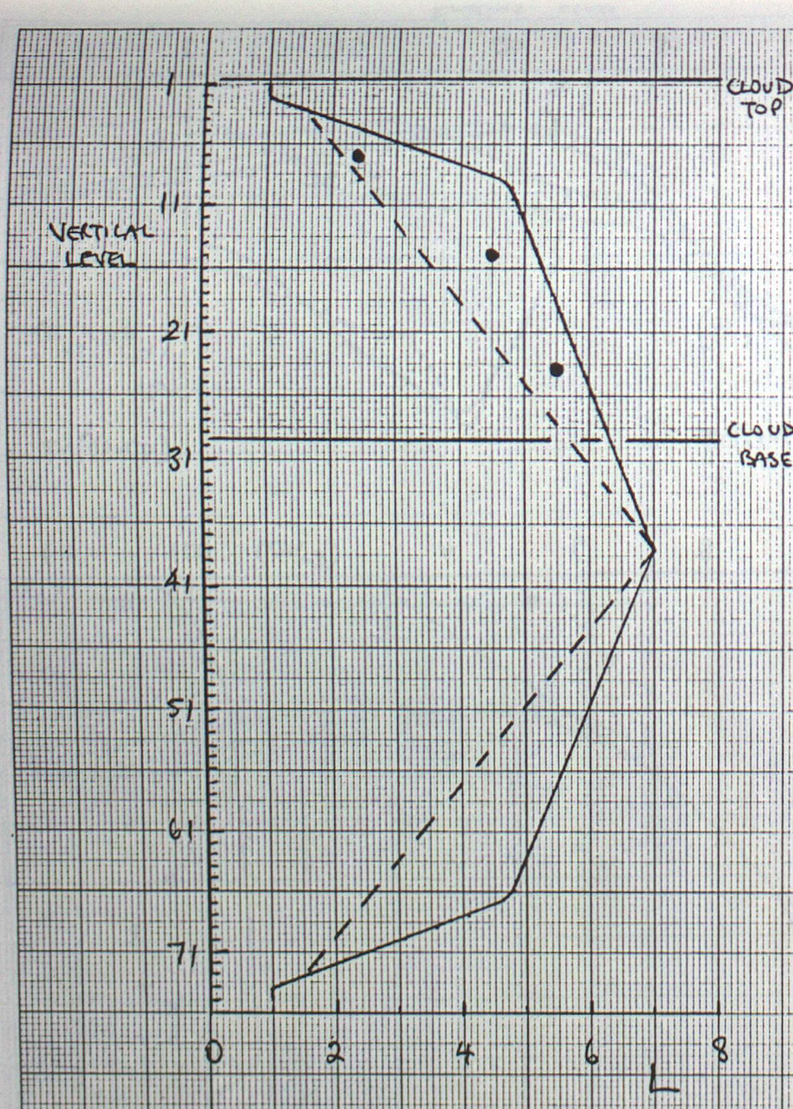
VERTICAL LEVEL
1
11
21
31
41
51
61
71
CLOUD TOP
CLOUD BASE
0
2
4
6
8
L

FIG 9

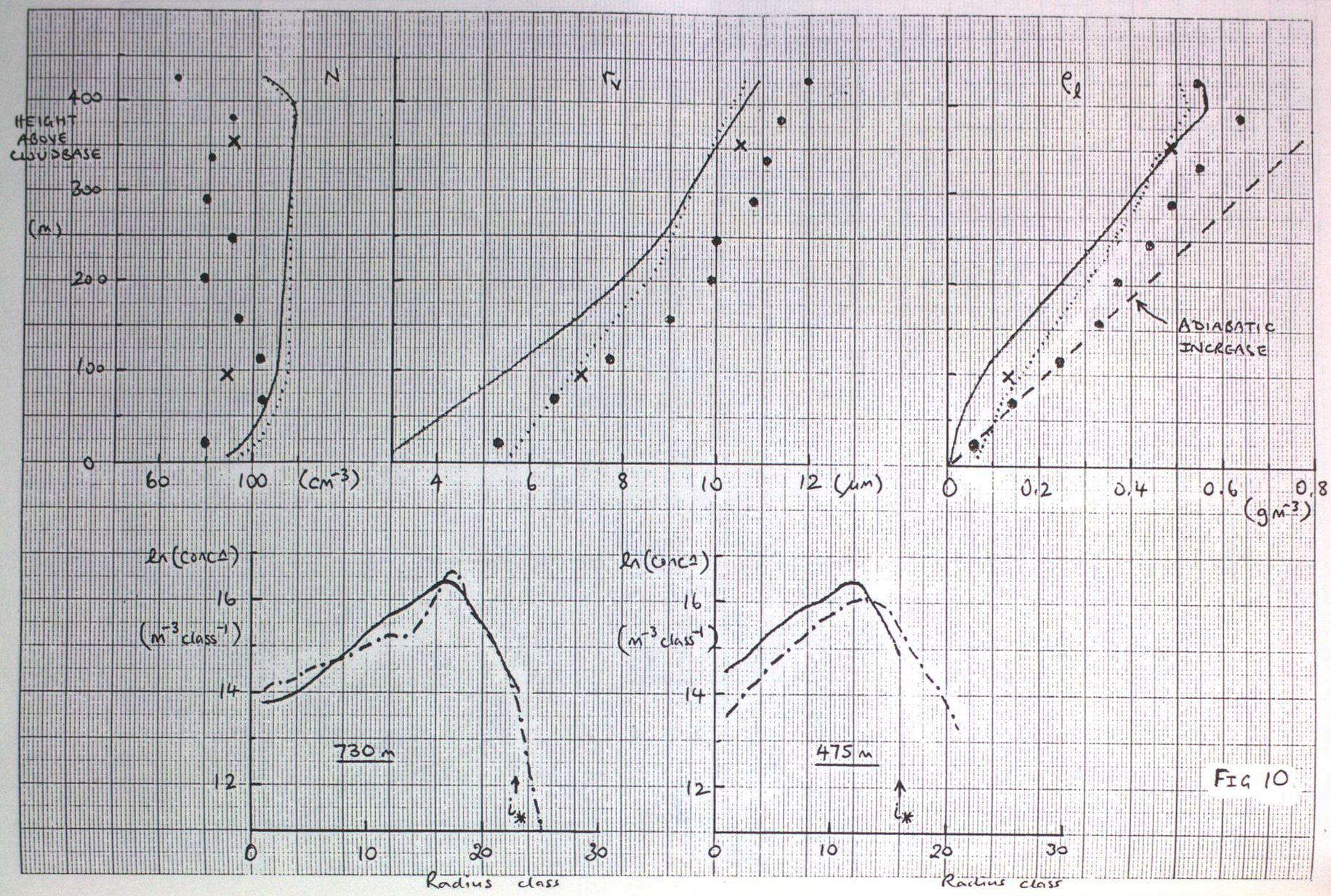
HEIGHT ABOVE CLOUDBASE (m)
400
300
200
100
0
N
60
100
(cm⁻³)
r_v
4
6
8
10
12 (μm)
e_l
0
0.2
0.4
0.6
0.8
(g m⁻³)
ADIABATIC INCREASE
ln (conc Δ)
(m⁻³ class⁻¹)
16
14
12
730 m
475 m
i_*
0
10
20
30
Radius class

FIG 10

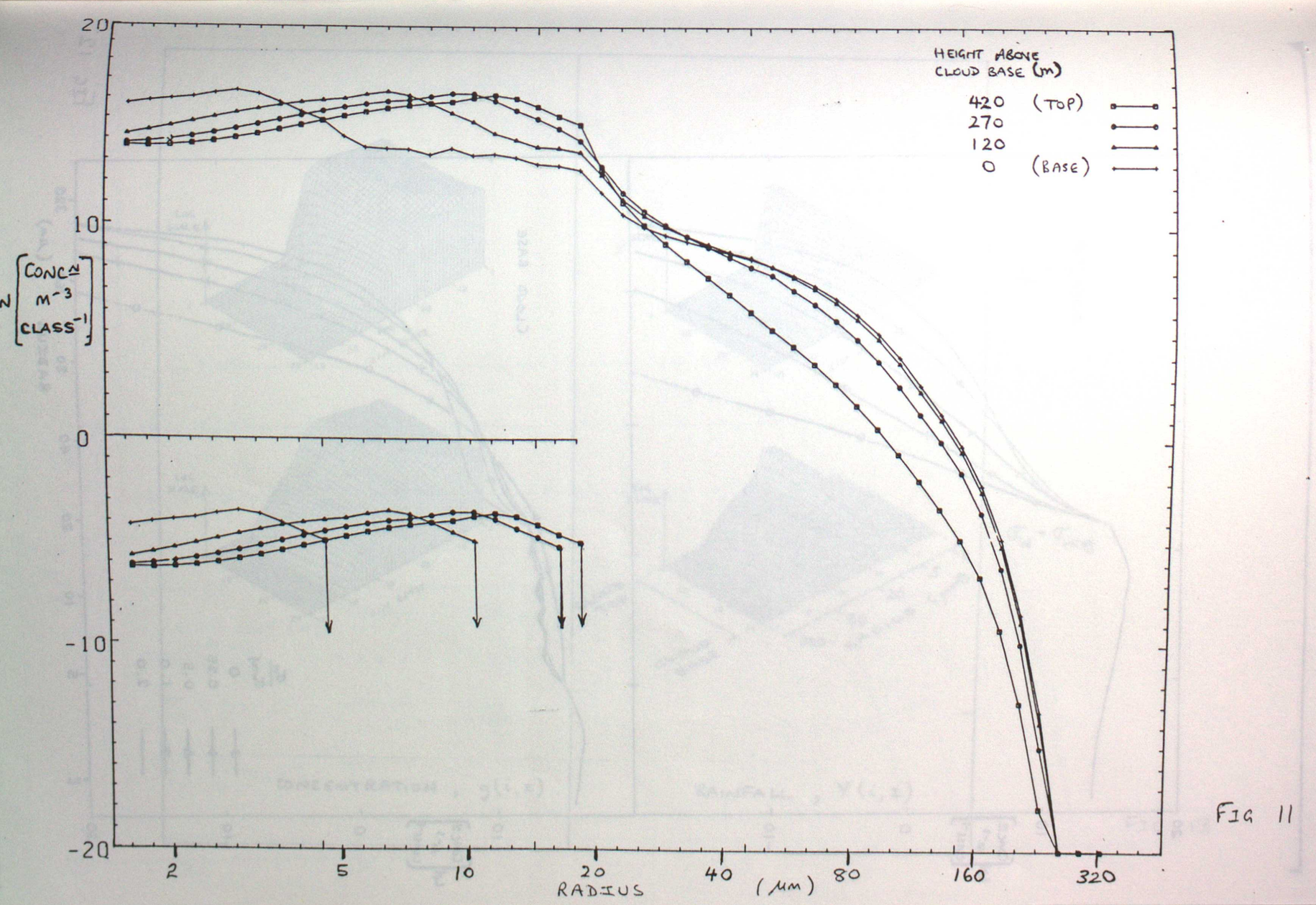
HEIGHT ABOVE CLOUD BASE (m)
420 (TOP)
270
120
0 (BASE)
LN [CONC N / m⁻³ CLASS⁻¹]
20
10
0
-10
-20
2
5
10
20
40
80
160
320
RADIUS (μm)

FIG 11

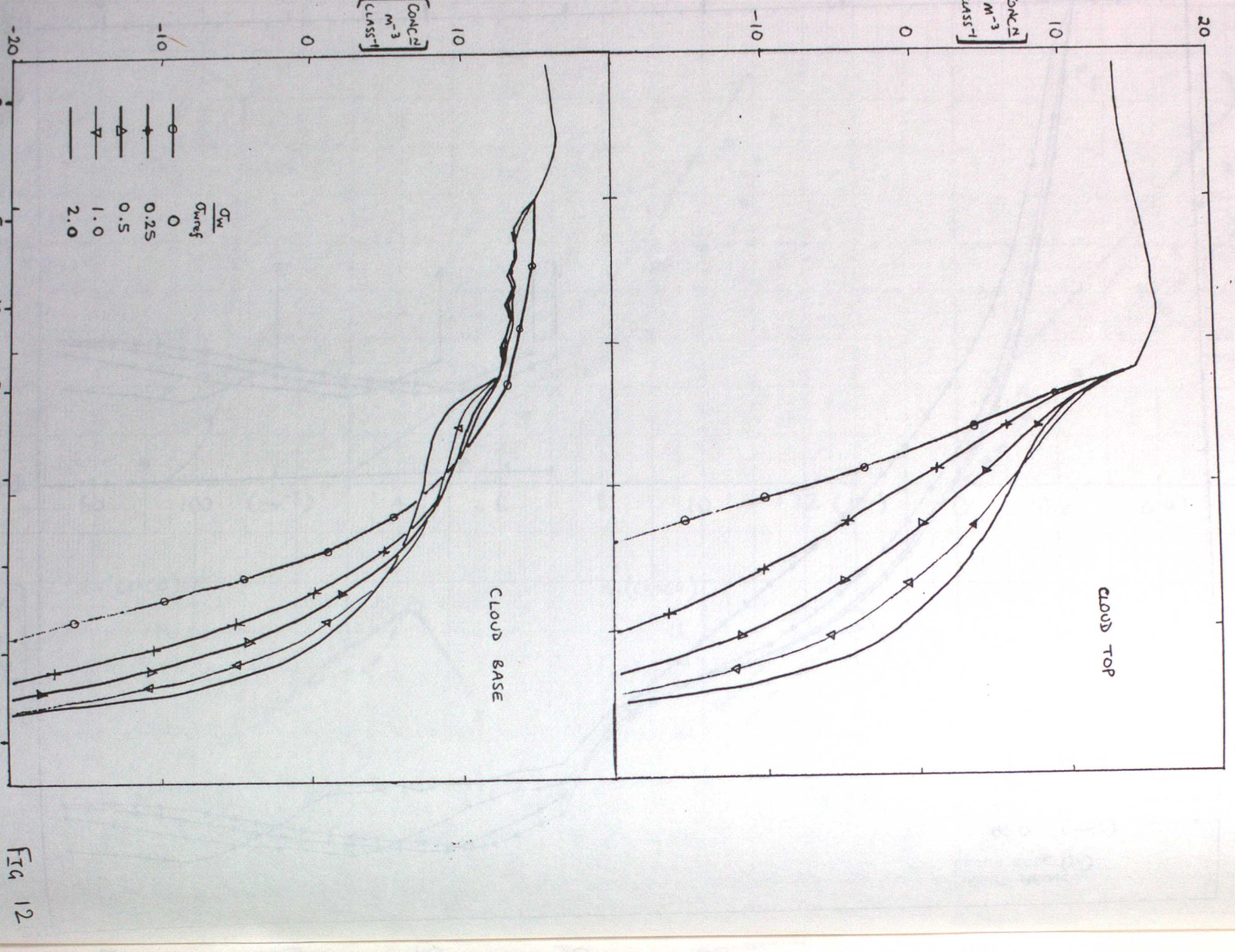
CLOUD TOP
CLOUD BASE
LN [CONCN m⁻³ CLASS⁻¹]
RADIUS (μm)
σw/σwref
0
0.25
0.5
1.0
2.0

FIG 12

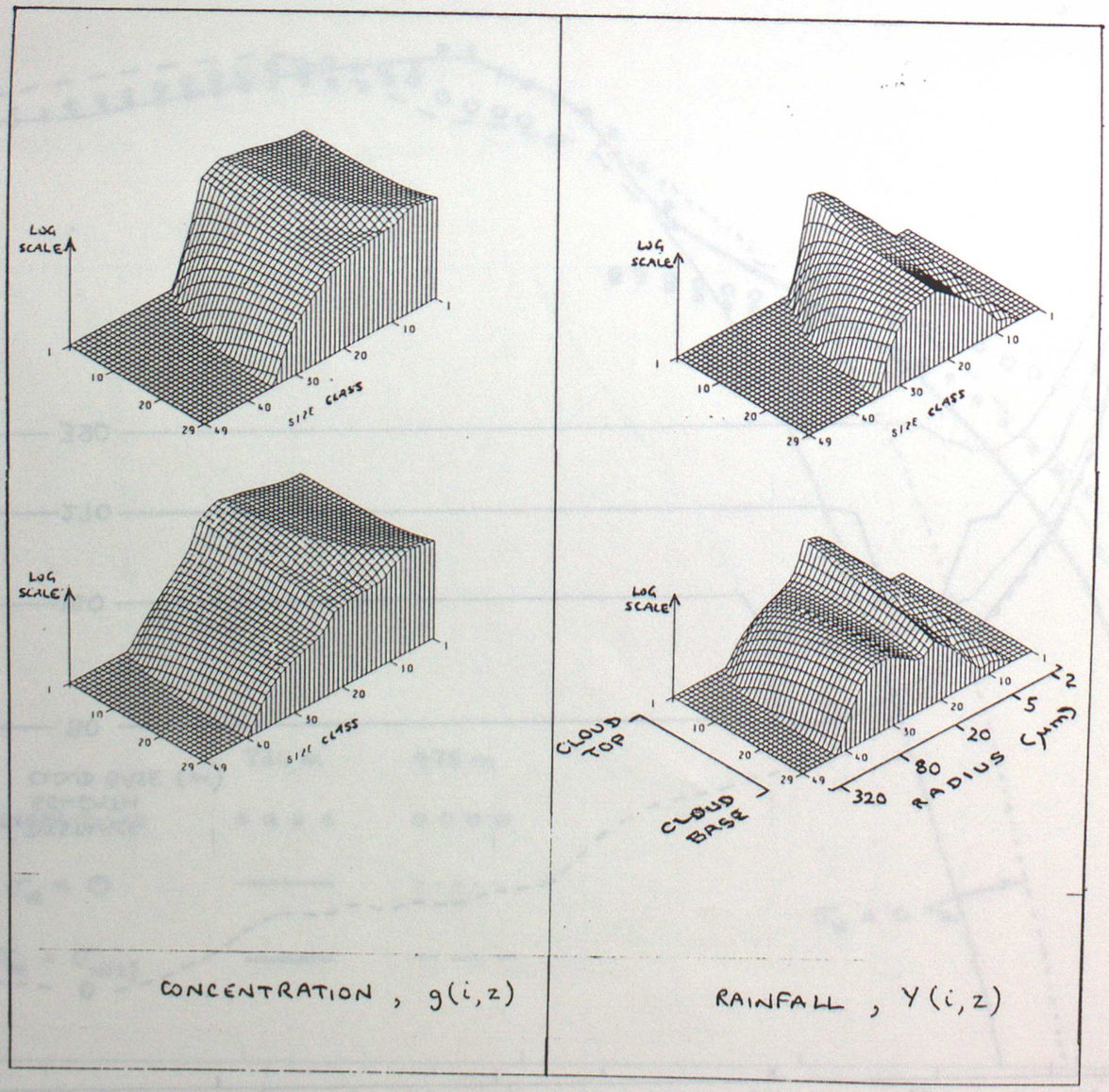
LOG SCALE
SIZE CLASS
CLOUD TOP
CLOUD BASE
RADIUS (μm)
CONCENTRATION , g(i,z)
RAINFALL , Y(i,z)
σw = 0
σw = σwref

FIG 13

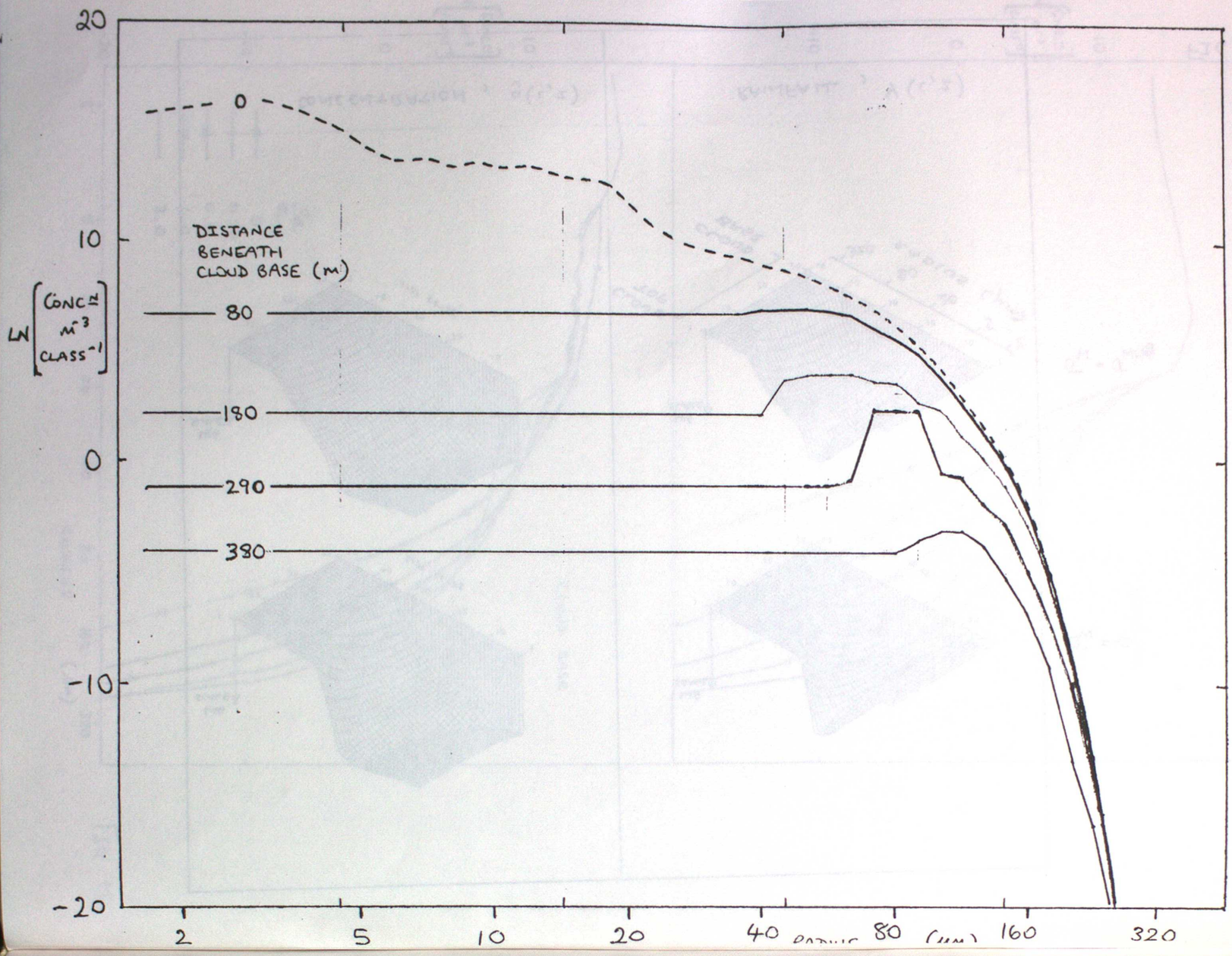
20
10
0
-10
-20
2
5
10
20
40
80
160
320
0
DISTANCE BENEATH CLOUD BASE (m)
80
180
290
380
LN [CONC^N m^-3 CLASS^-1]

FIG 14

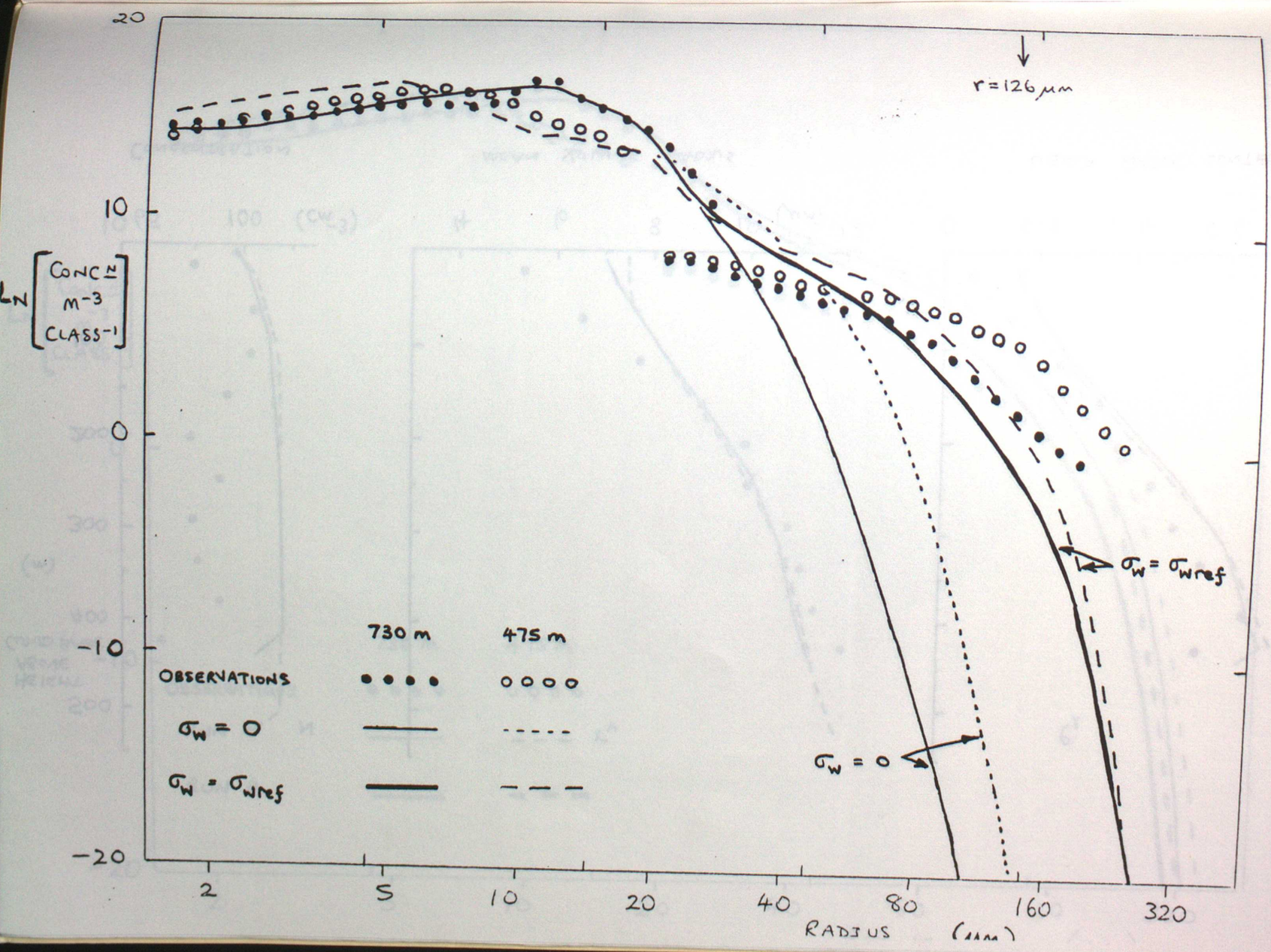
r=126 μm
730 m
475 m
OBSERVATIONS
σw = 0
σw = σwref
σw = σwref
σw = 0
LN [CONC^N m^-3 CLASS^-1]
RADIUS (μm)

FIG 15

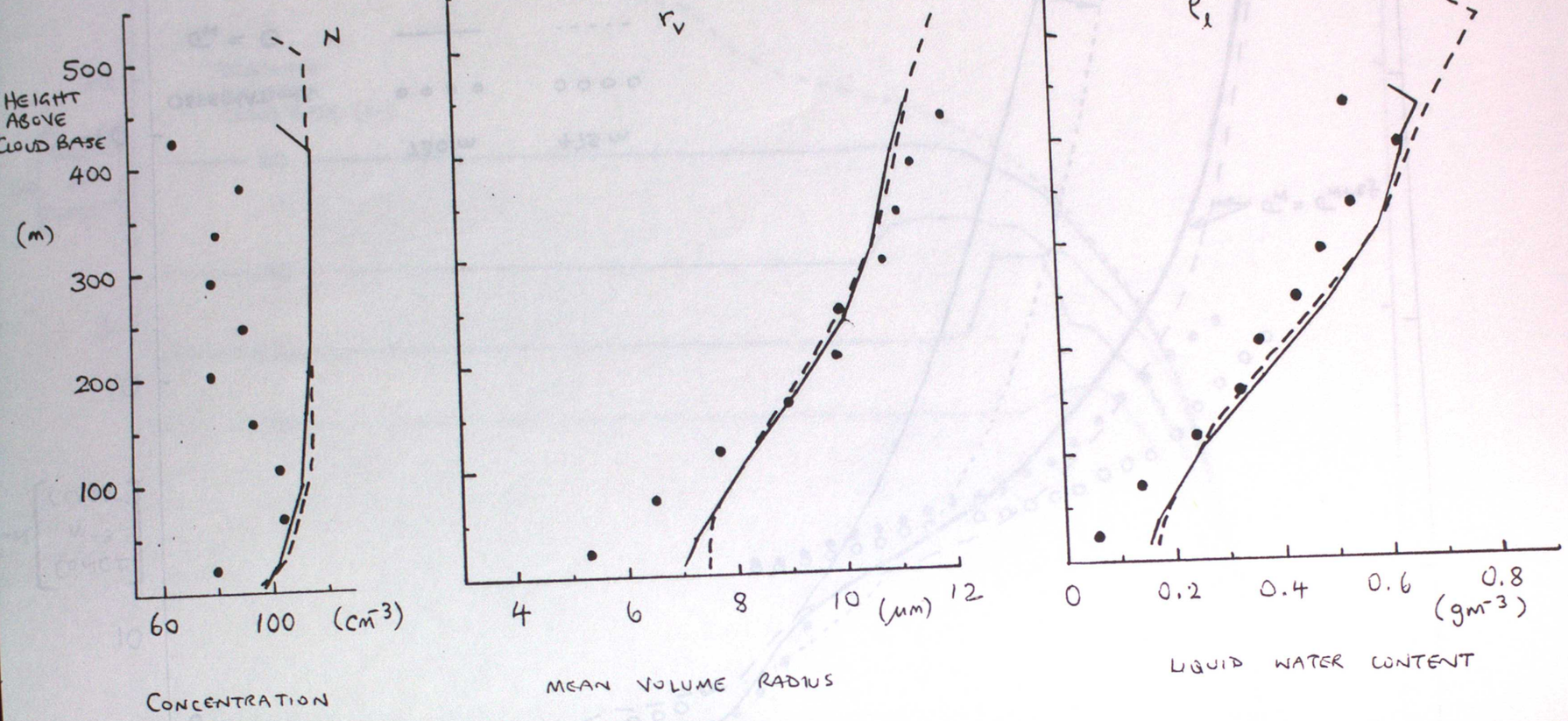
HEIGHT ABOVE CLOUD BASE (m)
500
400
300
200
100
N
60
100
(cm⁻³)
CONCENTRATION
r_v
4
6
8
10
12
(μm)
MEAN VOLUME RADIUS
ρ_l
0
0.2
0.4
0.6
0.8
(gm⁻³)
LIQUID WATER CONTENT

FIG 16

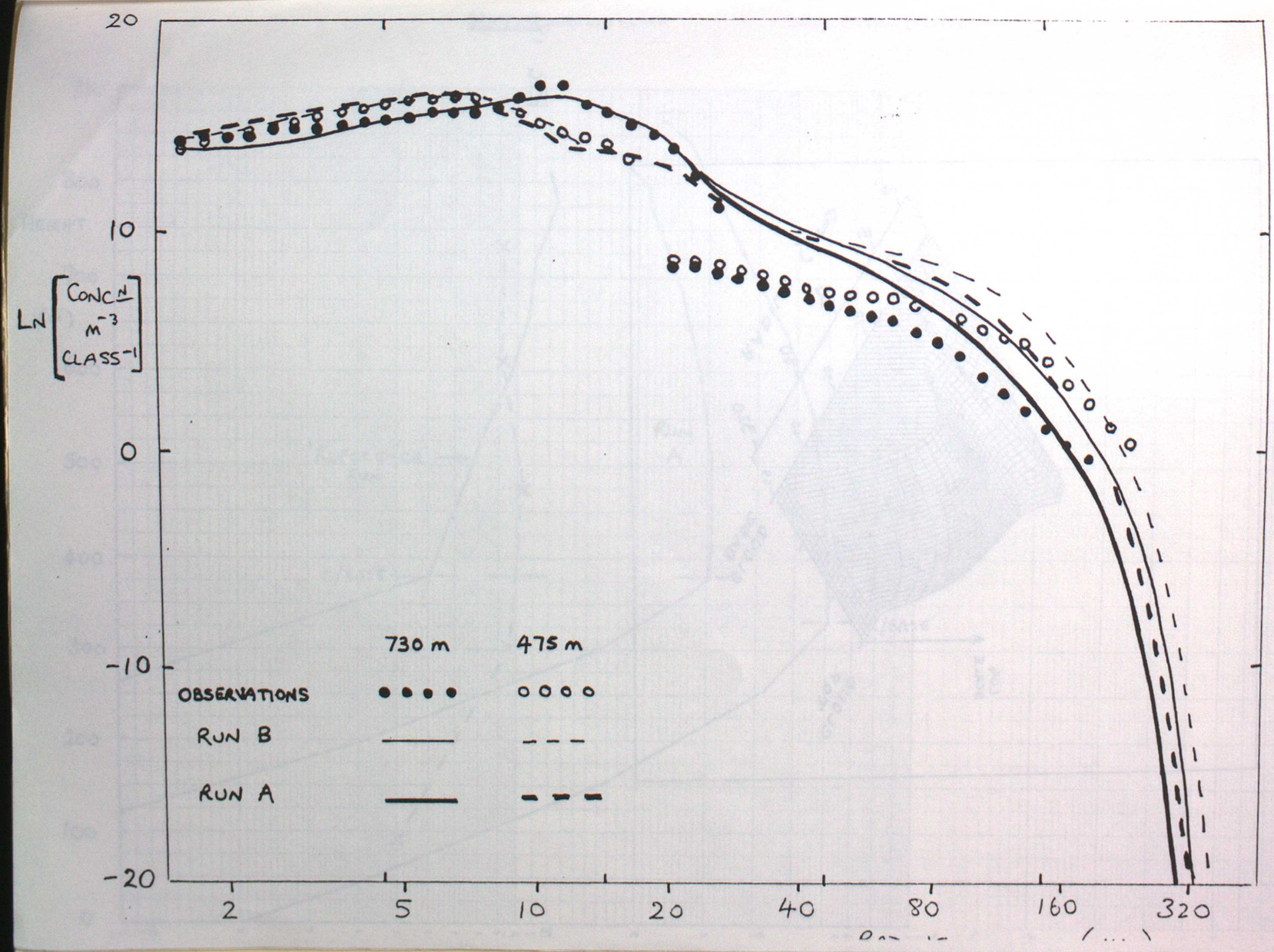
L_N [CONC^N m^{-3} CLASS^{-1}]
20
10
0
-10
-20
730 m
475 m
OBSERVATIONS
RUN B
RUN A
2
5
10
20
40
80
160
320

FIG 17

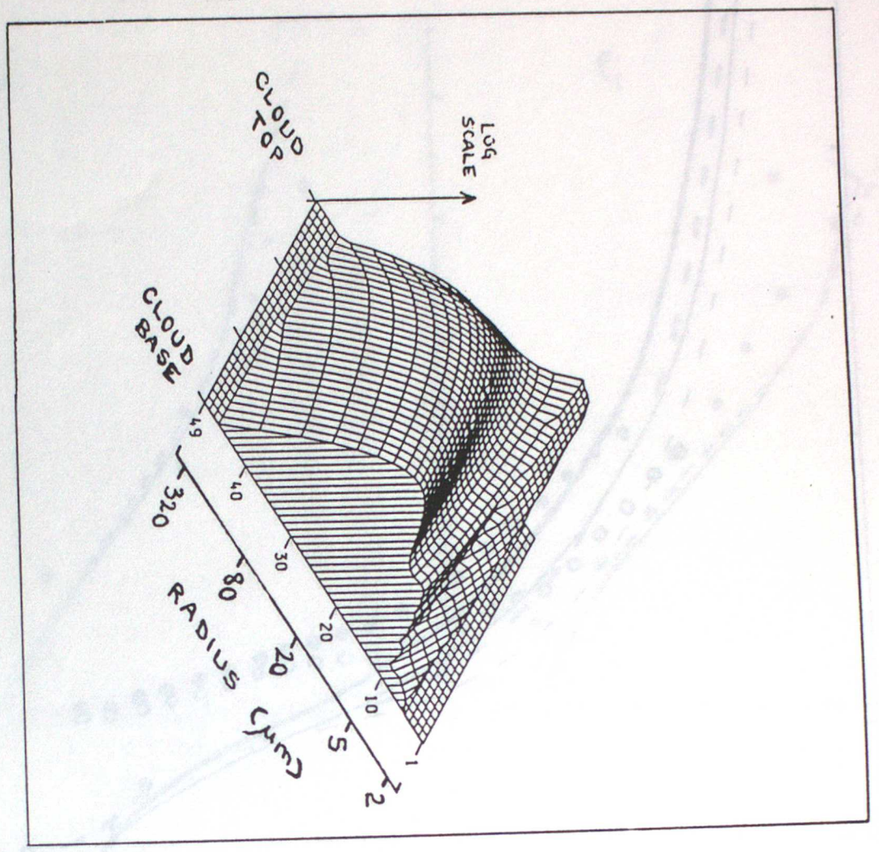

FIG 18

Chartwell Graph Data Ref. 5531 Log 3 Cycles x mm, ½ and 1 cm

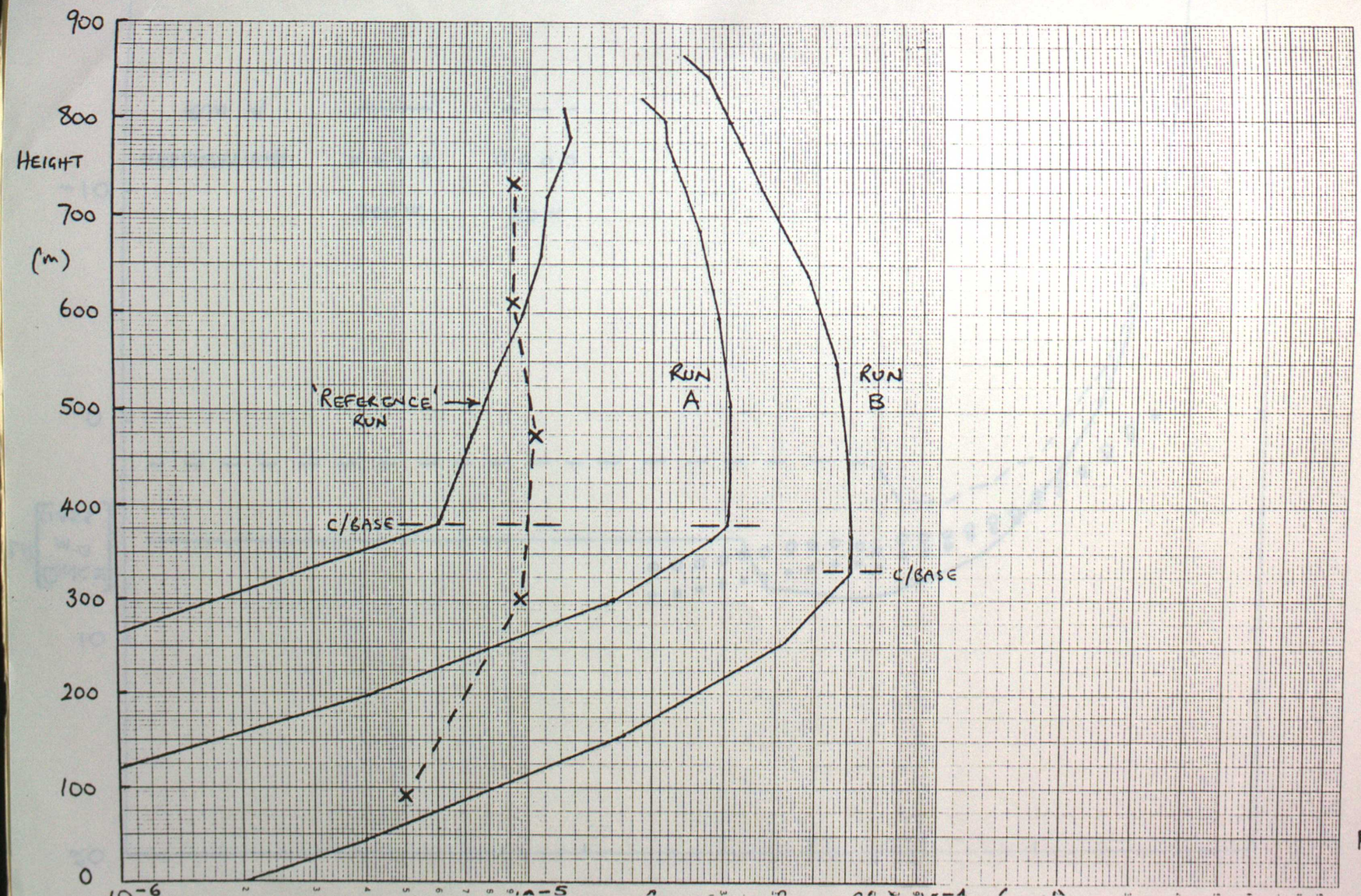

FIG 19

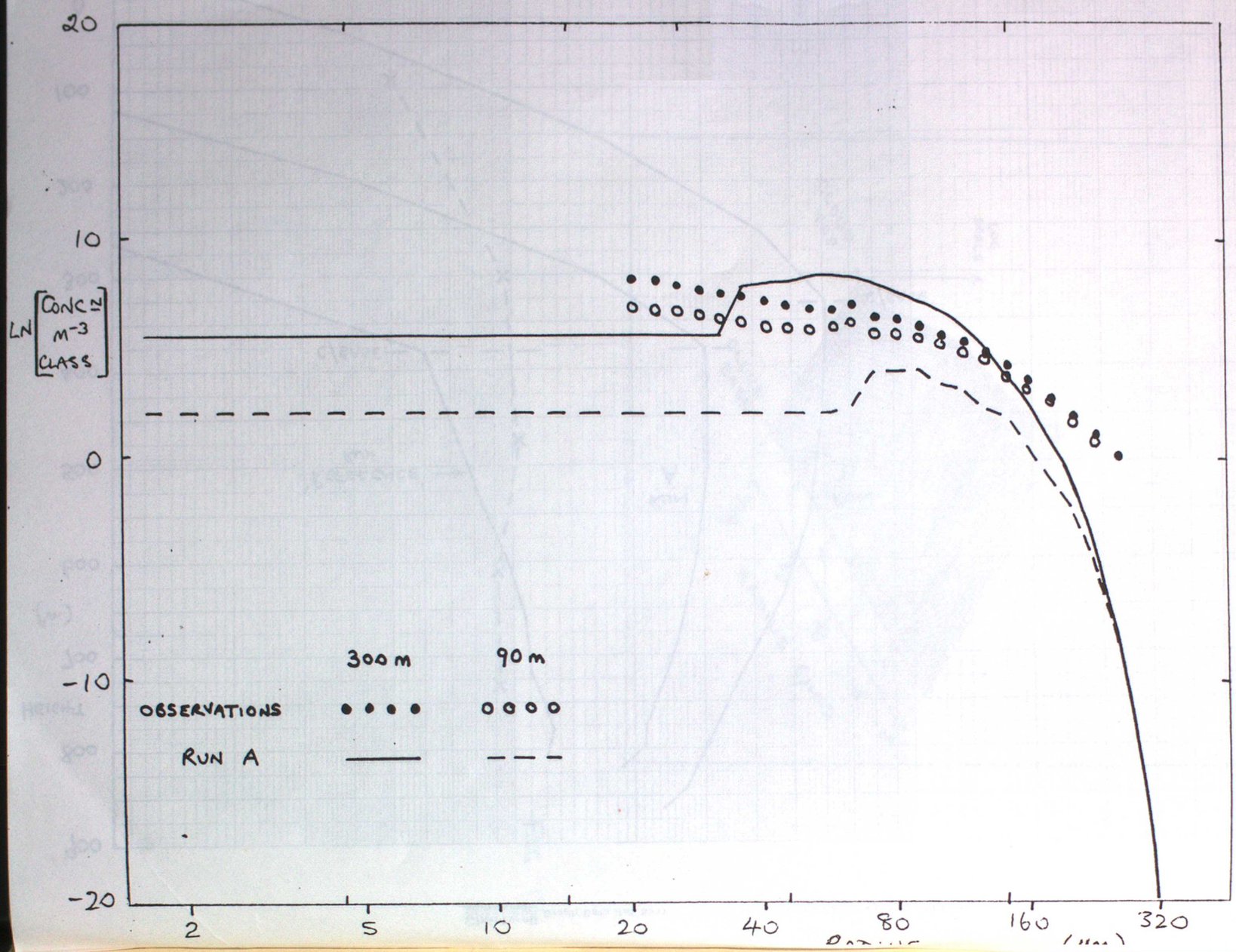
20
10
0
-10
-20
LN [CONC IN M-3 CLASS]
300 m
90 m
OBSERVATIONS
RUN A
2
5
10
20
40
80
160
320

FIG 20